

Emission Modeling of the Jet/Accretion Flow/Black Hole Systems in GRMHD

by

HAYLEY WEST, Department of Physics and Astronomy

THESIS

Presented to the Graduate Faculty of
The University of Texas at San Antonio
In Partial Fulfillment
Of the Requirements
For the Degree of

MASTER OF SCIENCE IN PHYSICS

COMMITTEE MEMBERS:

Richard Anantua, Ph.D., Chair
Eric Schlegel, Ph.D.
Vu Hoang, Ph.D.

THE UNIVERSITY OF TEXAS AT SAN ANTONIO
College of Sciences
May 2025

DEDICATION

I dedicate this work to my amazing and supportive parents, Laure and John, and my large and loving family. I would not be where I am today without your love and guidance and always pushing me to be the best version of myself throughout these many different chapters of my life. Despite living away from home since my undergraduate days, I have always felt the love, motivation, and support from hundreds of miles away and know you are always rooting for me. I also dedicate this work to my partner and best friend, Alex. Thank you for encouraging me to chase my goals as a scientist and being there every step of the way no matter what life threw at us. I also want to dedicate this to my younger self, who humbly had no idea what life would bring and would be so proud to see herself now.

ACKNOWLEDGEMENTS

There are many influential people I would like to acknowledge. I want to thank my research colleagues, Joaquin, Lani, and Brandon, who have mentored me as I began my journey into graduate school. I want to thank my advisor Dr. Richard Anantua for the continued support and guidance throughout my journey over the last two years and beyond. This group has set foundational groundwork as I begin my early career as an astrophysicist.

I want to thank my friends and peers at UTSA and in San Antonio who have taken me in and made me feel at home. A special thanks to Joaquin for being not just a colleague, but my best friend. There is never a dull moment when we are together, whether it be for work or fun.

I also want to thank my best friend, Anton. He has shaped who I am as a person from the first time we met in 2018 and has always been one of my biggest supporters throughout everything in the last 7 years whether we lived in the same town or half-way across the country. Thank you for always being in my corner.

This Masters Thesis/Recital Document or Doctoral Dissertation was produced in accordance with guidelines which permit the inclusion as part of the Masters Thesis/Recital Document or Doctoral Dissertation the text of an original paper, or papers, submitted for publication. The Masters Thesis/Recital Document or Doctoral Dissertation must still conform to all other requirements explained in the Guide for the Preparation of a Masters Thesis/Recital Document or Doctoral Dissertation at The University of Texas at San Antonio. It must include a comprehensive abstract, a full introduction and literature review, and a final overall conclusion. Additional material (procedural and design data as well as descriptions of equipment) must be provided in sufficient detail to allow a clear and precise judgment to be made of the importance and originality of the research reported.

It is acceptable for this Masters Thesis/Recital Document or Doctoral Dissertation to include as chapters authentic copies of papers already published, provided these meet type size, margin, and legibility requirements. In such cases, connecting texts, which provide logical bridges between different manuscripts, are mandatory. Where the student is not the sole author of a manuscript, the student is required to make an explicit statement in the introductory material to that manuscript describing the students contribution to the work and acknowledging the contribution of the other author(s). The signatures of the Supervising Committee which precede all other material in the Masters Thesis/Recital Document or Doctoral Dissertation attest to the accuracy of this statement.

May 2025

Emission Modeling of the Jet/Accretion Flow/Black Hole Systems in GRMHD

Hayley West, M.S
The University of Texas at San Antonio,

Supervising Professor: Richard Anantua, Ph.D.

Modeling emission in jet/accretion flow/black hole (JAB) systems is a crucial part of understanding the dynamical processes powering active galactic nuclei (AGN) known to reside in the center of a significant fraction of galaxies and underlie some of the most energetic processes in astrophysics. The Event Horizon Telescope (EHT) has made the first event-horizon scale images of a supermassive black hole (SMBH) - opening a new age of direct comparison of models of black hole influence on AGN processes and horizon-scale observation. While EHT's primary JAB $R-\beta$ Model has been rigorously tested, the alternative Critical- β Model has yet to be investigated in the same light despite promising advances. By modeling M87, a large, well-studied target, we can compare certain emission properties among alternative models. We also introduce a much-needed model to capture the phenomenology of shocks. We observe two flow states for the accreting plasma: Standard and normal evolution (SANE) and magnetically arrested disk (MAD). Computations are performed with two general relativistic radiative transfer (GRRT) codes to depict different morphological features throughout the evolution of the outflow and modeling of the spectral energy distribution (SED). We expand the Critical- β parameter space for M87 for the first time and discuss the implications. We find: 1.) As demonstrated in the library of images and corresponding spectra, the exponential decay in electron temperatures at high plasma β enables the Critical- β model to reduce bremsstrahlung contributions below observational constraints more efficiently than the $R - \beta$ prescription, and 2.) Episodic flux eruption morphologies associated with various peaks in magnetic flux and troughs in mass accretion for magnetically arrested disks.

TABLE OF CONTENTS

Acknowledgements	iii
Abstract	iv
List of Tables	viii
List of Figures	x
Chapter 1: Introduction	1
1.1 Background	1
1.2 JAB Systems	2
1.3 Event Horizon Telescope Collaboration	3
1.3.1 Very Long Baseline Interferometry	4
1.3.2 Next Generation-EHT	4
1.4 Motivation	4
Chapter 2: Observations of M87	6
2.1 Gamma-ray Observations	6
2.2 X-ray Observations	6
2.3 Optical-Infrared Observations	8
2.4 Radio-mm-submm Observations	8
Chapter 3: Theory	9
3.1 Plasma Physics and Magnetohydrodynamics	9
3.1.1 Magnetohydrodynamic Equations	10
3.1.2 Magnetohydrodynamic Effects	11
3.2 General Relativity	12
3.2.1 Einstein's Postulates	12

3.2.2	General Relativity Equations	12
3.2.3	Schwarzschild Solution	13
3.2.4	Kerr Solution in General Relativity	13
3.2.5	General Relativistic Magnetohydrodynamics	14
3.3	Radiative Processes	15
3.3.1	Synchrotron	15
3.3.2	Bremsstrahlung	16
3.3.3	Compton Scattering	17
3.4	Polarization	19
3.5	Radiative Transfer	20
3.5.1	Radiative Transfer Equation	20
3.5.2	Faraday Effects	21
Chapter 4: GRMHD Simulations		22
4.1	HARM Scheme	22
4.2	General Relativistic Radiative Transfer (GRRT)	23
4.2.1	IPOLE	23
4.2.2	GRMONTY	25
Chapter 5: Emission Models		27
5.1	Turbulent Heating Models	27
5.1.1	R- β Model	27
5.1.2	Critical- β Model	28
5.1.3	Alternative Models: Magnetic Reconnection and Shocks	29
5.2	Parameter Space for Investigation	30
5.2.1	R- β Parameters	31
5.2.2	Critical- β Parameters	31
5.3	Positron Effects	32

Chapter 6: Results and Model Comparisons	33
6.1 Comparison of Simulations with Observations	33
6.1.1 Comparison with Polarization Constraints	33
6.1.2 Comparison with β_2	34
6.2 Bremsstrahlung Contribution	36
6.2.1 MAD Effects	36
6.2.2 SANE Effects	38
6.3 Flux Eruption Events	40
6.4 Modeling with Positrons	43
Chapter 7: Conclusions and Future Directions	46
Appendix A: Full Polarization Tables	49
Appendix B: GRMONTY User Guide	52
Bibliography	57

Vita

LIST OF TABLES

5.1	Previously tested (f, β_c) values where most of the Sag A* investigation comes from the initial introduction of the Critical- β Model in Anantua et. al [16].	29
5.2	Values for free parameters in R- β model for all three timesteps. β_c is a constant always to be used as a value of 1.	31
5.3	Values tested for free parameters in Critical- β model for all three timesteps.	31
6.1	Median circular polarization for $ V _{net}$ and $\langle V \rangle$ for $20,000M - 30,000M$. The bold models satisfy the EHT limit of $-8.0 \cdot 10^{-3} V_{net} < 8.0 \cdot 10^{-3}$ and $0 \ll \langle V \rangle < 3.7 \cdot 10^{-2}$	34
6.2	Median linear polarization for $ m_{net} $ and $\langle m \rangle$. From [8], observational constraints were found to be $0.01 \leq m_{net} \leq 0.037$ and $0.057 \ll \langle m \rangle < 0.107$. The bold values refer to values that satisfy the linear polarization constraints.	34
6.3	Azimuthal structure mode β_2 for fiducial models at $T = 20,000M$. The observational constraints from EHT M87 Paper VII are in the range $0.04 \leq \beta_2 \leq 0.07$. The bold value refers to the fiducial model which satisfies the observational constraints.	35
6.4	Azimuthal structure mode β_2 for fiducial models at $T = 25,000M$. The observational constraints from EHT M87 Paper VII are in the range $0.04 \leq \beta_2 \leq 0.07$. The bold values refer to fiducial models which satisfy the observational constraints.	35
6.5	Azimuthal structure mode β_2 for fiducial models at $T = 30,000M$. The observational constraints from EHT M87 Paper VII are in the range $0.04 \leq \beta_2 \leq 0.07$. The bold value refers to the fiducial model which satisfies the observational constraints.	36

7.1	Values that have been tested in this thesis alongside values that will be tested for future investigations. Every row will be tested for all three fiducial timesteps of $T = 20,000M$, $25,000M$, and $30,000M$ as well as computed polarimetric images through IPOLE for both ion-electron plasma and electron-positron plasma.	48
A.1	Linear polarization for $ m_{net} $ and $\langle m \rangle$ for $T = 20,000M$. From [8], observational constraints were found to be $0.01 \leq m_{net} \leq 0.037$ and $0.057 \ll \langle m \rangle \ll 0.107$. The bold values refer to values that satisfy the linear polarization constraints.	49
A.2	Circular polarization for $ V _{net}$ and $\langle V \rangle$ for $T = 20,000M$ The bold models satisfy the EHT limit of $-8.0 \cdot 10^{-3}V_{net} < 8.0 \cdot 10^{-3}$ and $0 \ll V \gg 3.7 \cdot 10^{-2}$	49
A.3	Linear polarization for $ m_{net} $ and $\langle m \rangle$ for $T = 25,000M$. From [8], observational constraints were found to be $0.01 \leq m_{net} \leq 0.037$ and $0.057 \ll \langle m \rangle \ll 0.107$. The bold values refer to values that satisfy the linear polarization constraints.	50
A.4	Circular polarization for $ V _{net}$ and $\langle V \rangle$ for $T = 25,000M$ The bold models satisfy the EHT limit of $-8.0 \cdot 10^{-3}V_{net} < 8.0 \cdot 10^{-3}$ and $0 \ll V \gg 3.7 \cdot 10^{-2}$	50
A.5	Linear polarization for $ m_{net} $ and $\langle m \rangle$ for $T = 30,000M$. From [8], observational constraints were found to be $0.01 \leq m_{net} \leq 0.037$ and $0.057 \ll \langle m \rangle \ll 0.107$. The bold values refer to values that satisfy the linear polarization constraints.	50
A.6	Circular polarization for $ V _{net}$ and $\langle V \rangle$ for $T = 30,000M$ The bold models satisfy the EHT limit of $-8.0 \cdot 10^{-3}V_{net} < 8.0 \cdot 10^{-3}$ and $0 \ll V \gg 3.7 \cdot 10^{-2}$	51

LIST OF FIGURES

1.1	M87 as seen in linearly polarized light. The intense polarization lines around the black holes center showcase the magnetic field lines of the SMBH as presented by [5].	3
2.1	Composite image of the M87 JAB system across the entire electromagnetic spectrum as depicted in [12].	7
3.1	Depiction of helical motion of a particle under the effect of a uniform magnetic field.	15
3.2	Polarization ellipse with electric vector \mathbf{E} showing rotation of x and y electric field components coinciding with the principal axes. Image reproduced from [61].	20
4.1	An example R- β model of M87 for a MAD at $a = -0.5$ and $T = 30,000M$ for the 230 GHz emission. The left image clearly shows the strong magnetic field with the lack of EVPA. See subsection 4.2.1 for simulation information.	24
4.2	An example R- β model of M87 for a SANE at $a = -0.5$ and $T = 30,000M$ for the 230 GHz emission. The larger, chaotic EVPAs in the left image show the characteristic high density of a SANE. See subsection 4.2.1 for simulation information.	24
4.3	An example R- β SED of M87 for a MAD with $a = -0.5$ at $T = 30000M$ for the 230 GHz emission.	26
5.1	Comparison of Critical- β (dashed lines) against R- β (solid lines) for previously tested and reasonable parameters.	28

6.1	Spectra for MAD $a = -0.5$ and $T = 20,000M$. Left: SED for the Critical- β model showing lower bremsstrahlung contribution (purple) contributing to the validity of the model where $f = 0.5$ and $\beta_c = 1$. Right: SED for the R- β model where bremsstrahlung surpasses 10^{36} erg s $^{-1}$. R_{low} is the standard 1 and $R_{high} = 20$	37
6.2	Spectra for MAD $a = +0.94$ and $T = 25,000M$. Left: SED for the Critical- β model showing slightly lower bremsstrahlung contribution (purple) contributing to the validity of the model where $f = 0.5$ and $\beta_c = 1$. Right: SED for the R- β model where R_{low} is the standard 1 and $R_{high} = 20$	37
6.3	Spectra for MAD Critical- β at two different spins for $T = 20,000M$. SED is computed using the values $f = 0.5$ and $\beta_c = 0.1$. We observe once the β_c value is lowered from the standard 1.0, the bremsstrahlung contribution (purple) is one magnitude lower than its previous Critical- β model counterparts.	38
6.4	Spectra for SANE $a = -0.5$ and $T = 30,000M$. Left: SED for the Critical- β model showing extremely lower bremsstrahlung contribution (purple) where $f = 0.5$ and $\beta_c = 1$. Right: SED for the R- β model where bremsstrahlung surpasses 10^{39} erg s $^{-1}$ showing a magnitude of 6 difference. R_{low} is the standard 1 and $R_{high} = 20$	39
6.5	Spectra for SANE $a = +0.94$ and $T = 30,000M$. Left: SED for the Critical- β model showing extremely lower bremsstrahlung contribution (purple) where $f = 0.5$ and $\beta_c = 1$. Right: SED for the R- β model where bremsstrahlung surpasses 10^{37} erg s $^{-1}$ showing a magnitude of 4 difference. R_{low} is the standard 1 and $R_{high} = 20$	39

6.6	Temporal evolution of the MAD $a = -0.5$ simulation with horizon threading flux ϕ (red) and mass accretion rate \dot{m} (green) for $T = 10,000M - 30,000M$. The vertical dotted lines at $T = 17,730M, 25,000M$, and $27,110M$ show the sharp peaks in ϕ with the troughs in \dot{m} showing the flux eruption events for those individual timestamps.	40
6.7	For R- β $a = -0.5$ MAD at $T = 25,000M$, there is a noticeable flux eruption loop outside of the photon ring in the circular polarization image on the right.	41
6.8	Accompanying spectra for R- β $a = -0.5$ MAD at $T = 25,000M$	41
6.9	Temporal evolution of the MAD $a = +0.94$ simulation with horizon threading flux ϕ (red) and mass accretion rate \dot{m} (green) for $T = 10,000M - 30,000M$	42
6.10	Temporal evolution of the SANE $a = -0.5$ simulation with horizon threading flux ϕ (red) and mass accretion rate \dot{m} (green) for $T = 10,000M - 30,000M$	42
6.11	$R - \beta$ SANE model with jet inclusion from IPOLE with zero electron-positron pair fraction for $a = -0.5$ and $T = 20,000M$ for the 230 GHz emission.	44
6.12	$R - \beta$ SANE model with jet inclusion from IPOLE with equal electron-positron pair fraction for $a = -0.5$ and $T = 20,000M$ for the 230 GHz emission.	44
6.13	$R - \beta$ MAD model with jet inclusion from IPOLE with zero electron-positron pair fraction for $a = -0.5$ and $T = 20,000M$ for the 230 GHz emission.	45
6.14	$R - \beta$ MAD model with jet inclusion from IPOLE with equal electron-positron pair fraction for $a = -0.5$ and $T = 20,000M$ for the 230 GHz emission.	45

CHAPTER 1: INTRODUCTION

1.1 Background

Astrophysics has entered a new age where theoretical predictions can be matched against observational evidence to provide the most accurate modeling of high energy phenomena. With the introduction of general relativistic magnetohydrodynamics (GRMHD) simulations, theoretical models of high-energy astrophysical phenomena can be rigorously tested against observational data.

It is an exciting decade in astronomy and astroparticle physics with major discoveries such as LIGO's first detection of gravitational waves from a black hole merger and the long-awaited discovery of the Higgs boson, which gives particles mass. The Event Horizon Telescope Collaboration (EHT) fits in line with these monumental discoveries, delivering the first image of a black hole (BH). April of 2019 was a historic period when the first image was announced [32], and since then even the SMBH at our own galactic center has been imaged with better resolution for the first time on the horizon scale.

BHs are known as compact objects that have a gravitational pull strong enough that not even light can escape. Characterized by the existence of an event horizon, or essentially the boundary at which light or matter can no longer escape, a BH is parameterized by:

$$R = \frac{2GM}{c^2}, \quad (1.1)$$

where G is the gravitational constant, c is the speed of light, and M is the mass of the BH.

First conceptualized dating back to 1794 [50], John Mitchell proposed the idea of a "black hole" by stating that if a star's diameter exceeded the Sun's by a factor of 500, a compact object could form where light could not escape. Following Mitchell, Einstein's renowned theory of general relativity (GR) (theoretically detailed in Section 3.2) described spacetime in its completeness accounting for the large-scale gravitational effects of the cosmos. The existence of BHs was a direct consequence of his theory despite not being discovered for another 60 years [28].

1.2 JAB Systems

While BHs can be conceptualized as their own entity within a galactic center, they work as a system in what we coin the jet/accretion flow/black hole or JAB system. This accounts for the relativistic jet outflow from a BH as well as the turbulent accretion flow, as they all work in tandem when observing and modeling the system. This systematic description is common in AGNs such as M87. Used to describe the massive size of a BH located in the center of most large galaxies, a supermassive black hole is a BH with a mass $M_{BH} \geq 10^5 M_{\odot}$ and can range to a mass of over a billion times the mass of the Sun [35]. The formation of these galactic giants is still an open question.

There are two distinct flow states to describe the accreting plasma that surrounds the BH: magnetically arrested disk (MAD) and standard and normal evolution (SANE). The distinction can be characterized by the magnetic flux through the horizon in Gaussian units:

$$\Phi_{BH} = \frac{1}{2} \int |B'| dA_{\phi\theta}. \quad (1.2)$$

Φ_{BH} is the magnetic flux interior to the BH equator [54]. A MAD state occurs when the strong magnetic field disrupts the axisymmetric accretion flow, first conceptualized in [54]. The inflow of material is inhibited by magnetic pressure near the BH. SANEs have a negligible magnetic field flux, alternatively consisting of a higher plasma density [36, 55]. This distinction is demonstrated in Figure 4.1 and Figure 4.2.

In addition to describing the flow states, we can also analytically describe the accretion flow of the JAB system. A radiatively inefficient accretion flow (RIAF) describes the luminosity in the low-Eddington regime, a common, broad label given to many SMBHs. A more specific type of RIAF would be an advection-dominated accretion flow (ADAF) where the accreting gas is still radiatively inefficient and the accretion flow is underluminous [55].

1.3 Event Horizon Telescope Collaboration

EHT is an international collaboration comprised of 11 current radio telescopes for the purpose of compiling observational data and imaging of BHs. EHT's goal, alongside capturing images of these densely compact objects, is to test the effects of GR in a new light, including how gravity interacts around a BH and the direct detection of matter in orbit around it at near the speed of light.

Imaging these sources has led to valuable constraints on both M87 and Sagittarius A* (Sgr A*), including the mass of their BH and limits for both circular and linear polarization. The addition of these observables has enabled the continuing accuracy of new theoretical models.

Since the release of the first imaged BHs, EHT has already provided more detailed images of both M87 and Sgr A* in polarized light, as can be seen in Figure 1.1. These improvements depict the structure of the magnetic field swirling around the center of the BH and provide us with a direct probe of the magnetic field structure of these JAB systems.

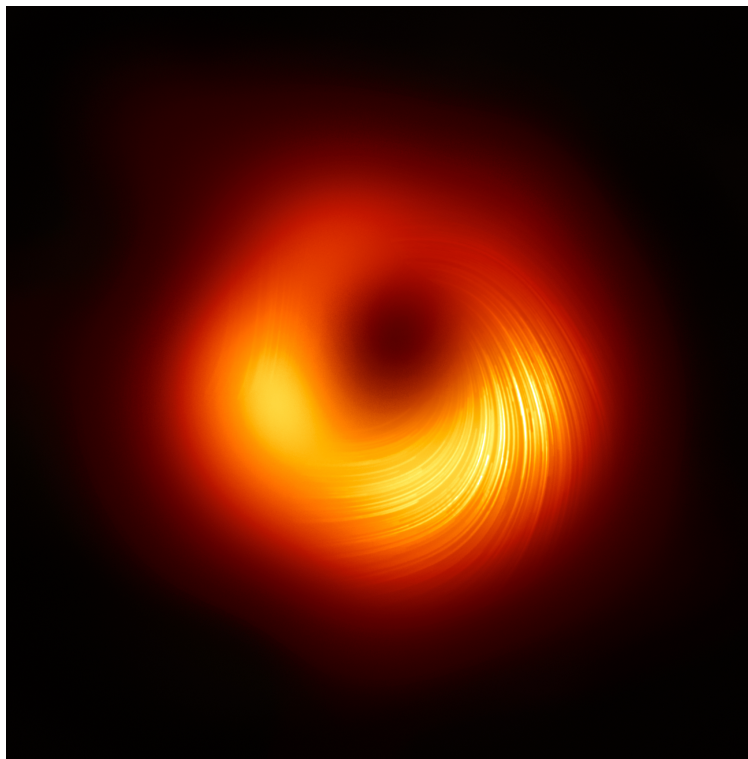


Figure 1.1: M87 as seen in linearly polarized light. The intense polarization lines around the black holes center showcase the magnetic field lines of the SMBH as presented by [5].

1.3.1 Very Long Baseline Interferometry

Very Long Baseline Interferometry (VLBI) is the instrumental practice in radio astronomy of collecting a signal through a radio source from multiple different radio telescopes, either on Earth or in space. EHT employs the method of VLBI to construct the images of BHs from observational data through an ‘Earth-sized’ interferometer to measure the size of emission regions of Sgr A*, M87, and soon to be other large extragalactic sources. With the improvement of other observational radio systems such as Very Long Baseline Array (VLBA) and Very Large Array (VLA), more accurate data will be extrapolated from these sources in the future.

1.3.2 Next Generation-EHT

Next Generation-EHT (ng-EHT) is a promising extension of EHT with the aim of building on their advanced technology to bring better images and observational data of BHs. In addition, their hope to expand EHT’s current array of telescopes brings promise to enhance the current findings of their predecessor. While still employing the technique of VLBI, their investigation will test the workings of magnetic fields around BHs as well as advanced testing of GR.

The Black Hole Explorer (BHEX) will be a monumental space-based telescope designed to provide supplemental data that the ground-base telescopes are not able to provide. As an anticipated project until its expected launch date in 2031, BHEX will hope to image the photon ring around BHs, measure the spin of these objects, and peer deeper into the universe to observe further and larger SMBHs .

1.4 Motivation

In [14], the methodology of Observing JAB systems is described, and a brief summary of results for M87 and Sgr A* is presented. In the series [16, 17] detailed comparisons of Sgr A* and M87 are done with focused parameter space surveys. Here, we revise the previous investigations and add the latest observations by EHT.

- Extend EHT's M87 investigations of the models including our own pass-fail tables to include a larger parameter space
- Extend [17] Critical- β parameter search and find equitable comparison for the R- β model
- Comparison with currently available observational data from EHT, including circular and linear polarization and β_2 structural mode
- Observing the temporal evolution of the fiducial simulation in order to understand the morphology of the system

In addition to continuing to further the already established Observing JAB Simulations program, the groundwork will be laid for new investigations.

- Future horizon-scale targets, e.g., 3C 279, already observed by multi-wavelength campaigns will be considered as subjects of this methodology, and best bet models will be proposed
- New plasma physics will be motivated and described in new emission models

Although much about plasma turbulence is still unknown, this deep-dive investigation into emission modeling allows us to draw further conclusions on the viability of these turbulent heating models. This investigation will aid in the further analysis of a larger parameter space of EHT targets.

CHAPTER 2: OBSERVATIONS OF M87

Messier 87, or M87, is a massive elliptical galaxy and arguably one of the most well-studied JAB sources to date. It is located within the Virgo cluster at a distance of 16.8 ± 0.8 Mpc. Based on the observations from its powerfully prominent jet observed to be misaligned from our line of sight, M87 is classified as an FRI misaligned BL-Lac blazar. It is the first JAB source to be imaged [32].

We adopt a SMBH mass of $6.5 \pm 0.7 \times 10^9 M_{\odot}$ with an associated Eddington luminosity of 8×10^{40} W and energy scale of 1.2×10^{57} J [7, 17]. The JAB system is estimated to have a dimensionless mass accretion rate of $\dot{m} \equiv \dot{M}/\dot{M}_{Edd} \approx 10^{-5}$ [6]. M87 has a powerful jet powered by the Blandford-Znajek mechanism [19]. This mechanism requires that the BH have a nonzero spin in accordance with EHT constraints and causes Poynting flux of electromagnetic energy due to the interactions with the spin of the BH and its magnetic field. Despite its large jet and massive central BH, M87 is very underluminous and often modeled as a RIAF.

2.1 Gamma-ray Observations

M87 was the first extragalactic source detected at very high energies, where *Fermi* Large Area Telescope (LAT) reported detection of gamma-ray emission up to 30 GeV with a luminosity of 4.9×10^{41} erg s⁻¹ [1]. Earlier studies in the high-energy regime found no evidence of significant variability [1], only variable TeV emission on yearly timescales [2]. Although in recent years, full investigations of the *Fermi*-LAT dataset shows evidence for high energy (>100 MeV) gamma-ray flux variability on a month-type timescale [18].

2.2 X-ray Observations

Chandra X-Ray Observatory observed M87 in the X-ray band with subarcsecond angular resolution, determining the X-ray emission emission of the jet to be synchrotron radiation with almost certainty [67].

Residing near the center of the Virgo Cluster, M87's position centers it in a weak cooling

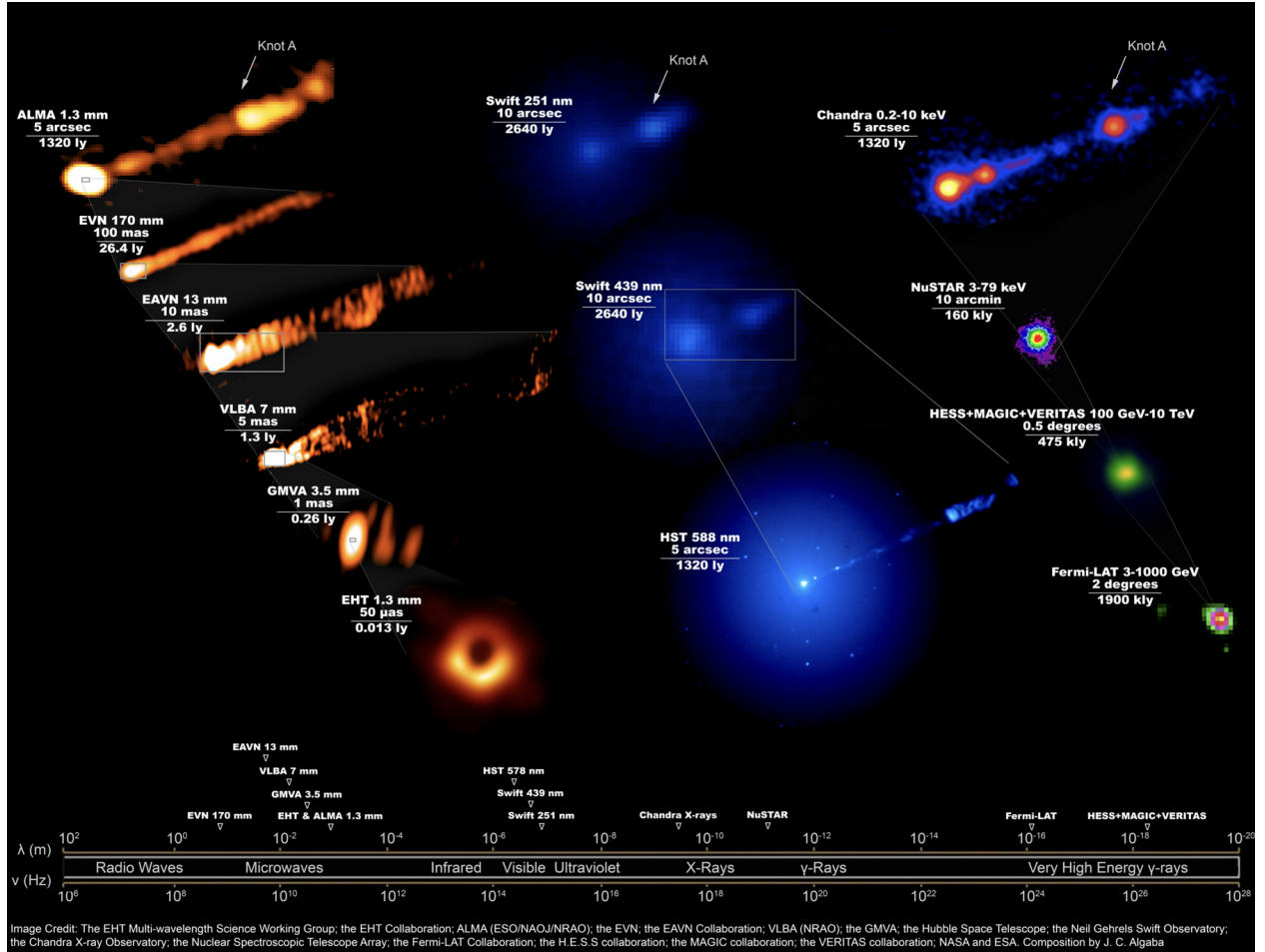


Figure 2.1: Composite image of the M87 JAB system across the entire electromagnetic spectrum as depicted in [12].

flow region with an associated X-ray luminosity of 10^{36} W [24]. The X-ray emission is largely symmetric around M87's nucleus, as well as strongly peaked at its center [24]. This suggests that the hot gas is maintained in a rough dynamical equilibrium state and sets an associated estimate of the jet power at $L_{jet} = 5 \times 10^{36}$ W [17].

Recent observations have found the 2-10 keV band luminosity of M87's core to be $8.8 \pm 0.4 \times 10^{40}$ erg s^{-1} [10], showing a significant increase in flux relative to 2017 observations first found to be $4.8 \pm 0.2 \times 10^{40}$ erg s^{-1} [10]. Observations from the EHT Multi-wavelength (MWL) Science Working Group narrowed a photon index of $\Gamma = 2.06^{+0.10}_{-0.07}$ [10].

2.3 Optical-Infrared Observations

The *Hubble Space Telescope* has observed the optical jet of M87 in great detail, revealing its spectrum of the jet to be considerably steeper in the optical band than radio with 40 percent variability between 1993 and 1997 [57].

Although quite faint in the infrared, *Spitzer Space Telescope* is the perfect instrument for observing the emission at this wavelength. Thermal emission from cool dust at $T = 55\text{K}$ reveals spectra from *Spitzer* with an IR luminosity of $\sim 10^{39} \text{ erg s}^{-1}$ [58].

Investigations from the EHT MWL Group found the core to dominate the innermost region of M87 within the optical band [10]. Optical flux densities for the core region were found within the v , b , and u bands within a radius of 5" and corrected for host galaxy contamination [10].

2.4 Radio-mm-submm Observations

As a prominent radio galaxy, many notable observations of M87 and its powerful accompanying jet have been published. Notable publications include pilot monitoring at 22 GHz displaying superluminal motion up to $\sim 1.6c$ [39], a Global mm-VLBI Array 86 GHz observation showing a limb-brightening jet base [44], and an 86 GHz image exhibiting strong Faraday rotation effects and around 20 percent linear polarization [40].

These combined observations allow for better resolution of the jet morphology and show the radio jet to be modestly relativistic. M87's jet is quite variable, roughly parabolic, and collimated within $z \sim 30M$ [17].

Observations obtained at 3.5-mm showed the spatially resolved radio core of M87 alongside an edge-brightened jet [47]. Marginal variability was noted from the 1.3-mm flu density between observations from 2017 and 2018 [47].

CHAPTER 3: THEORY

3.1 Plasma Physics and Magnetohydrodynamics

Plasma, a highly energetic state of ionized matter, often appears in astrophysical contexts as magnetized, turbulent, and possessing diverse equilibrium states. Plasma energization through turbulent dissipation is the cornerstone of plasma physics, where electron-ion pair energization is a fundamental result of plasma turbulence, although it is a poorly understood subject [70].

The heating prescription of weakly collisionless plasma described in [41] has a sharp transition between electrons preferentially heated at $\beta \leq 1$ to protons preferentially heated at $\beta > 1$. Plasma β , the controlling parameter of heating partition, is defined as

$$\beta = \frac{P_{gas}}{P_{magnetic}}, \quad (3.1)$$

where magnetic pressure in a magnetic field is defined as $P_B = \frac{B^2}{2\mu_0}$. In the low- β plasmas ($\beta \ll 1$), magnetic field pressure dominates leading to an unstable disk and magnetic reconnection occurring. In the high- β regime, gas pressure dominates, and the accretion disk behaves more fluid-like.

For simplicity, we assume a thermal electron distribution function expressed in units of electron rest mass described by a Maxwell-Jüttner distribution:

$$\Theta_e = \frac{k_B T_e}{m_e c^2}. \quad (3.2)$$

Θ_e indicates how relativistic the electrons are where $\Theta_e \ll 1$ are non-relativistic and $\Theta_e \geq 1$ are relativistic. Equation 3.2 is determined by the electron-ion temperature ratio ($R = T_i/T_e$):

$$T_i = \frac{2m_p u}{3k_B \rho (2 + R)}, \quad (3.3)$$

where u is the internal energy density and ρ is the rest-mass density [4].

Turbulent heating of collisionless plasma in a semi-relativistic regime fits well with the time-dependent empirical formula from first-principle physics

$$\frac{\Delta E_e}{\Delta E_i} \approx \left(\frac{\rho_e}{\rho_i}\right)^{2/3}, \quad (3.4)$$

where $(\rho_e/\rho_i)^{2/3}$ is a non-trivial function of θ_{i0} and β_0 [70]. Equation 3.4 is supportive evidence towards the well-tested idea that electron-ion dominated plasmas will evolve towards an equilibrium two-temperature state, as described in Section 5.1 for different two-temperature state turbulent heating models.

3.1.1 Magnetohydrodynamic Equations

Describing the equations that govern magnetohydrodynamics (MHD) is critical to understanding the physics behind plasma. MHD couples Maxwell's equations with hydrodynamics, describing an electrically conducting fluid [42]. Here, we define a fluid as a phenomenon emerging from a large collection of particles with locally defined variables such as temperature, density, and pressure.

MHD is equipped with the constraint equation $\nabla \cdot \mathbf{B} = 0$, which governs the spatial structure of the \mathbf{B} -field. The first equation for idealized MHD is the continuity equation for mass conservation describing the time evolution of the mass density ρ :

$$\frac{\partial \rho}{\partial t} + \nabla \cdot (\rho \mathbf{V}) = 0. \quad (3.5)$$

The motion of the fluid can be described through the Euler equation as

$$\rho \left[\frac{\partial \mathbf{V}}{\partial t} + (\mathbf{V} \cdot \nabla) \mathbf{V} \right] = -\nabla P + \mathbf{j} \times \mathbf{B}, \quad (3.6)$$

where \mathbf{j} is the electric current density, \mathbf{V} is the plasma velocity, P is the thermodynamic pressure.

To obtain the induction equation, we can start with Ohm's law:

$$\mathbf{j} = \sigma \mathbf{E}', \quad (3.7)$$

where σ is the electrical conductivity and \mathbf{E}' is the electric field denoted in the rest frame where $\mathbf{E}' = \mathbf{E} + \mathbf{V} \times \mathbf{B} = \frac{1}{\sigma} \mathbf{j}$. Assuming perfect conductivity ($\sigma \rightarrow \infty$), the electric field then becomes:

$$\mathbf{E} = -\mathbf{V} \times \mathbf{B}. \quad (3.8)$$

Using Maxwell's equation $\nabla \times \mathbf{E} = -\frac{\partial \mathbf{B}}{\partial t}$, we can conclude the induction equation as:

$$\frac{\partial \mathbf{B}}{\partial t} = \nabla \times (\mathbf{V} \times \mathbf{B}). \quad (3.9)$$

3.1.2 Magnetohydrodynamic Effects

There are various effects of MHD including Alfvén's Theorem, or the frozen-flux theorem to describe an ideal MHD. Frozen-flux theorem implies that the magnetic flux in the plasma is a conserved quantity and is directly described in Equationrefeq:perfcon [9]. Hannes Alfvén described perfect conductivity as the idea that the magnetic field lines were "frozen" into the conducting fluid or the plasma and is used as a way to describe the motion of the magnetic field lines [9].

Alfvén also first described the idea of plasma supporting wave-like variations within the magnetic field as a consequence of MHD. It is characterized by a low-frequency oscillation of ions within the plasma that is transverse in nature parameterized by:

$$v = \frac{v_A}{\sqrt{1 + v_A^2/c^2}}, \quad (3.10)$$

where $v_A \equiv B/\sqrt{\mu_o \rho}$ is the Alfvén wave group velocity [9].

Magnetic reconnection is another natural effect of MHD that involves the breaking and reconnecting of magnetic field lines in a plasma and takes place in the magnetosphere of BHs. Since BHs are magnetized, the oppositely directed magnetic field lines reconnect at a substantial fraction of Alfvén speed. Although first introduced to describe solar flares, this concept has paved the

way for extreme electrodynamic bodies like neutron stars and BHs to be described by this same concept.

3.2 General Relativity

The Theory of General Relativity is the core to understanding physics behind the most dense bodies in our universe. It has predicted many important phenomena before they were even observed, including gravitational waves and BHs.

At its simplest explanation, GR explains how gravity affects the fabric of a four-dimensional spacetime. It is a fundamental way to geometrically describe how intervals in the four-component spacetime are measured in the presence of mass [21].

3.2.1 Einstein's Postulates

In the early 1900s, Einstein's Theory of both Special and General Relativity shaped the field of physics. GR was a specific case of his astounding special theory of relativity, in which gravity was not accounted for. Published in 1905, special relativity had two main postulates that translated into GR: 1. The laws of physics are the same in all inertial frames of reference, and 2. The speed of light is invariant in any inertial frame of reference [29].

GR unified inertial and accelerating reference frames. To fully explain the effects of gravity, Einstein developed the Principle of Equivalence stating: "All local, freely falling, non-rotating laboratories are fully equivalent for the performance of all physical experiments" [21].

3.2.2 General Relativity Equations

The important field equation of GR can be written as

$$G_{\mu\nu} + \Lambda g_{\mu\nu} = kT_{\mu\nu}, \quad (3.11)$$

where $T_{\mu\nu}$ is the stress-energy tensor, Λ is the cosmological constant, and $k = 8\pi G/c^4$ is Einstein's gravitational constant [28]. The Einstein tensor, $G_{\mu\nu}$, is defined as

$$G_{\mu\nu} = R_{\mu\nu} - \frac{1}{2}Rg_{\mu\nu}, \quad (3.12)$$

where R is the scalar curvature parameter and $g_{\mu\nu}$ is the metric tensor. $R_{\mu\nu}$ is the Ricci curvature tensor and characterizes how a body moves in the curvature of spacetime.

3.2.3 Schwarzschild Solution

Schwarzschild's metric describes a non-rotating, uncharged BH for which Equation 1.1 describes its event horizon. He published the first exact solution to Einstein's field equations [64], expressed as a metric describing the spacetime around a spherically symmetric point mass detailed as

$$ds^2 = -\left(1 - \frac{2GM}{rc^2}\right)c^2dt^2 + \left(1 - \frac{2GM}{rc^2}\right)^{-1}dr^2 + r^2d\theta^2 + r^2\sin^2\theta d\phi^2, \quad (3.13)$$

where ds^2 is related to the metric tensor of Equation 3.12 by $ds^2 = g_{\mu\nu}dx^\mu dx^\nu$.

When the radial coordinate of a star's surface has collapsed to

$$r_s = \frac{2GM}{c^2}, \quad (3.14)$$

this is known as the Schwarzschild radius [21]. Once collapsed at this point, the star is now a BH. At the point on the spherical surface where $r = r_s$, the BH is enclosed by the event horizon, past which is known as the point where light cannot escape.

3.2.4 Kerr Solution in General Relativity

As GR gained traction, a cornerstone publication by Kerr described a rotating BH in spacetime, a generalization to the Schwarzschild metric [43]. While the Kerr metric still describes a rotating

point mass, the addition of angular momentum yields a more complicated solution:

$$ds^2 = -\left(1 - \frac{r_s r}{\Sigma}\right) c^2 dt^2 + \frac{\Sigma}{\Delta} dr^2 + \Sigma d\theta^2 + \left(r^2 + a^2 + \frac{r_s r a^2}{\Sigma} \sin^2 \theta\right) \sin^2 \theta d\phi^2 - \frac{2r_s r a \sin^2 \theta}{\Sigma} c dt d\phi. \quad (3.15)$$

Here, $\Delta = r^2 - r_s r + a^2$, $\Sigma = r^2 + a^2 \cos^2 \theta$, and $a = J/Mc$ have been used for simplicity. The Kerr metric includes an important aspect to GR known as frame-dragging since the astrophysical body is rotating. This phenomenon drags objects in the vicinity of the BH into the gravitating body's rotation simply due to the existing curvature of spacetime [43].

Despite many solutions in the literature to describe the spacetime of BHs, the most fundamental characteristic to all BHs is the inclusion of an event horizon. Beyond this barrier, nothing is radiated from inside the BH's horizon, causing the discovery of their existence to be a mere theory for decades to come.

3.2.5 General Relativistic Magnetohydrodynamics

General relativistic corrections to MHD have become vital for theoretical testing of GR and for accurate testing of high-energy astrophysical plasmas. GRMHD is usually conservative in stress-energy-momentum ($\nabla_\mu T_\nu^\mu = 0$) and mass ($\nabla_\mu(\rho u^\mu) = 0$) [3] (see chapter 4 for applications). The governing equations of ideal GRMHD, written as a set of conservation laws, are as follows:

$$\partial_t(\sqrt{-g}\rho u^t) = -\partial_i(\sqrt{-g}\rho u^i), \quad (3.16)$$

$$\partial_t(\sqrt{-g}T_\nu^t) = -\partial_i(\sqrt{-g}T_\nu^i) + \sqrt{-g}T_\lambda^k \Gamma_{\nu k}^\lambda, \quad (3.17)$$

$$\partial_t(\sqrt{-g}B^i) = -\partial_j(\sqrt{-g}(b^j u^i - b^i b^j)), \quad (3.18)$$

in addition to a no-monopoles constraints $\partial_i(\sqrt{-g}B^i) = 0$. Here, ρ is defined as the rest-mass density of the fluid, b^μ is the magnetic induction four-vector, and u^μ is the fluid four-velocity (for

specific applications to our simulations with GRMHD, see Section 4.1).

With the addition of GR to the MHD equations, the plasma near a SMBH is relativistically affected. Consequences such as time dilation and length contraction can no longer be ignored. The advent of GRMHD has provided influential models to astrophysical phenomena such as gamma-ray bursts, SMBH feedback, BH mergers, and many more.

3.3 Radiative Processes

3.3.1 Synchrotron

Particles accelerated by a magnetic field tangled around BHs radiate, but for non-relativistic velocities, the nature of the radiation is called cyclotron radiation. The frequency of emission is interchangeable with the frequency of gyration in the B-field. The frequency of the gyration is quantified as

$$\omega_B = \frac{qB}{\gamma mc}, \quad (3.19)$$

where $\gamma = (1 - v^2/c^2)^{-1/2}$ is the Lorentz factor.

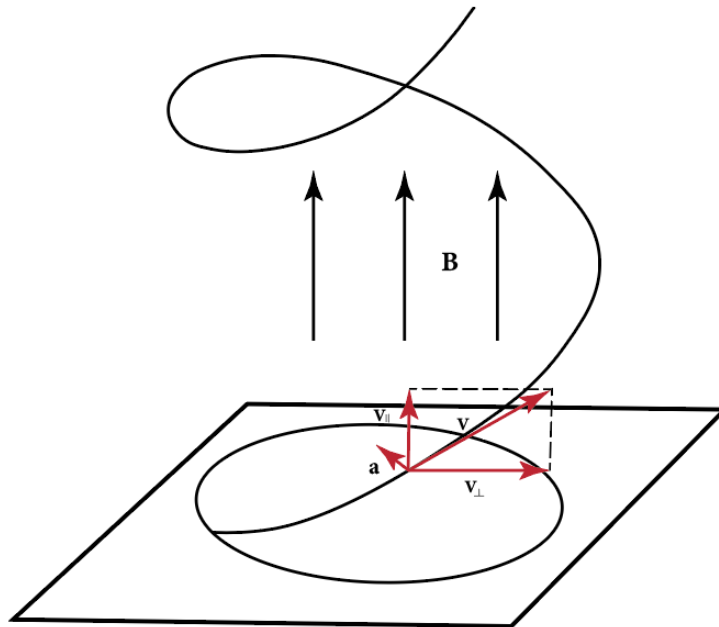


Figure 3.1: Depiction of helical motion of a particle under the effect of a uniform magnetic field.

However, for extreme relativistic particles the frequency spectrum is much more complex and can extend to many times Equation 3.19, known as synchrotron radiation where the particles travel in a helical path along the magnetic field lines, as can be seen in Figure 3.1 [61]. Synchrotron radiation will be strongly beamed in the direction of the relativistically charged particle. This creates a cone of width $\approx 1/\gamma$ radians [62].

Relativistic Corrections

The relativistic regime follows the evolution of electrons from cyclotron to synchrotron emission, namely, when v/c begins to increase, ω_B begins to contribute [61] and the spectra are no longer continuous. The electric field from a non-relativistic charged particle is sinusoidal over time with a Dirac delta function related power spectrum. A highly relativistic particle's electric field no longer resembles a sine function. The form now resembles sharp pulses repeated at intervals of $T = 2\pi/\omega_B$.

For a smooth distribution of particles, the polarization due to synchrotron radiation will be partially linearly polarized. The polarization of the emission will be described by the perpendicular ($P_{\perp}(\omega)$) and parallel ($P_{\parallel}(\omega)$) constituents of the power per unit frequency parameterized as:

$$\Pi(\omega) = \frac{P_{\perp}(\omega) - P_{\parallel}(\omega)}{P_{\perp}(\omega) + P_{\parallel}(\omega)}. \quad (3.20)$$

3.3.2 Bremsstrahlung

Bremsstrahlung, also known as free-free emission within plasmas, is the radiation due to the acceleration of a charged particle in a Coulomb field of another charge [61]. Although bremsstrahlung is sub-dominant in ADAFs, it is still an important radiative process to discuss due to its effect on observed spectra, as demonstrated in our results.

Electron-positron pairs created by background photon collisions produced at $h\nu \geq m_e c^2$ can influence the structure of the accretion flow in regions where the existing plasma density is less than the Goldreich and Julian density [68]. This results in bremsstrahlung having the ability to dominate

the X-ray and gamma-ray observed emission even if the bremsstrahlung itself is energetically negligible, as seen in [4].

For electron-ion dominated emission, the emission coefficient equation can be written as

$$j_\nu = \frac{8q_e^6}{3m_e^2c^4} \sqrt{\frac{2\pi}{3}} \Theta_e^{-1/2} n_e n_i e^{-h\nu/k_B T_e} \bar{g}_{ff}, \quad (3.21)$$

where \bar{g}_{ff} is the thermally averaged Gaunt factor correction for the relativistic regime [61]. For our simulation GRMONTY, described in Section 4.2.2, the electron-ion bremsstrahlung in the code uses the emission coefficient described in Equation 3.21 [26].

Although the radiation emitted from plasma is described as free-free radiation in which the electrons are free before and after the emission of a photon, bremsstrahlung can also be bound-bound or free-bound radiation. When radiated in a bound-bound state, the electron moves between two bound states as the radiation is described by discrete spectral lines. Free-bound describes a combination process where a free electron recombines with an ion.

Effect on Spectra

For an optically thin, geometrically thick accretion flow such as M87, the dominant processes radiated from the disk are bremsstrahlung and synchrotron. Bremsstrahlung is often neglected in the literature due to the energetically dominant synchrotron processes that occur for low-accreting systems [68]. Bremsstrahlung still has the ability to dominate the gamma-ray and X-ray spectra and affect observables, even when minimally energetic as seen in [4], and becomes increasingly important as the mass accretion rate increases.

3.3.3 Compton Scattering

When photons consist of sufficiently low energies ($h\nu \ll mc^2$), the scattering of radiation from the free charges is defined by the classical case of Thomson scattering [61]. While the majority of the scattering is elastic, quantum effects can appear through either: 1. Differing kinematics of the scattering or 2. Modification of the cross sections.

The former scenario describes a case where the photon possesses a momentum and energy, causing the collision to become inelastic due to recoil from the charge. In terms of the wavelength, this new relation can be shown as

$$\lambda_1 - \lambda = \lambda_c(1 - \cos(\theta)), \quad (3.22)$$

where $\lambda_c \equiv \frac{h}{mc}$ is the Compton wavelength ($\approx 2.43 \cdot 10^{-12}\text{m}$), θ is the scattering angle, λ is the initial wavelength, and λ_1 is the final wavelength.

The later scenario for quantum effects occurs when the cross-section is reduced, thereby increasing the energy of the photon. This relation for unpolarized radiation is described by the Klein-Nishina formula [61]:

$$\frac{d\sigma}{d\Omega} = \frac{r_0^2}{2} \frac{\epsilon_1^2}{\epsilon^2} \left(\frac{\epsilon}{\epsilon_1} + \frac{\epsilon_1}{\epsilon} - \sin^2(\theta) \right). \quad (3.23)$$

Inverse Compton

For moving charges, inverse Compton scattering may occur when low-energy photons collide with a relativistic electron thereby transferring energy to the photon [61]. Inverse Compton scattering can occur when electrons carry a higher kinetic energy or temperature than the incident photons. In the relativistic regime, this increase in energy is of order γ^2 .

When quantifying radiation lost due to inverse Compton and synchrotron, both mechanisms can be described by the same ratio as the photon energy density and magnetic field energy density [61]. This ratio is depicted as:

$$\frac{P_{synch}}{P_{compt}} = \frac{U_B}{U_{ph}}. \quad (3.24)$$

The spectral index for inverse Compton emission is identical to synchrotron emission as seen through the relation $s = (p - 1)/2$ [61].

Inverse Compton becomes an important emission mechanism when dealing with production of

X-rays and gamma-rays in the JAB systems. Electrons with relativistic energies in astrophysical bodies can upscatter low-energy photons via inverse Compton scattering [61].

3.4 Polarization

Light will be polarized when emitted in hot regions of magnetized space and the polarization depends on the orientation of the magnetic fields in these high-energy astrophysical plasmas. The Stokes polarization parameters (I, Q, U, V) are the observables of the polarized field in terms of its total intensity, introduced by George Gabriel Stokes in 1852 [65]. For a monochromatic wave, or purely elliptical polarization, the four Stokes parameters are related by

$$I^2 = Q^2 + U^2 + V^2, \quad (3.25)$$

where I is proportional to the total intensity or energy flux of the wave, V is the circular polarization, and Q and U are the conditions for linear polarization, measuring the orientation relative to the x-axis. [61]. $Q = U = 0$ is the condition required for circular polarization, and $V = 0$ is the condition for linear polarization. A more descriptive way to show the Stokes equations for the polarization through the principal axes of an ellipse, as seen in Figure 3.2, is

$$I = E_{0x}^2 + E_{0y}^2, \quad (3.26)$$

$$Q = E_{0x}^2 - E_{0y}^2, \quad (3.27)$$

$$U = 2E_{0x}E_{0y}\cos(\delta), \quad (3.28)$$

$$V = 2E_{0x}E_{0y}\sin(\delta), \delta = \delta_y - \delta_x. \quad (3.29)$$

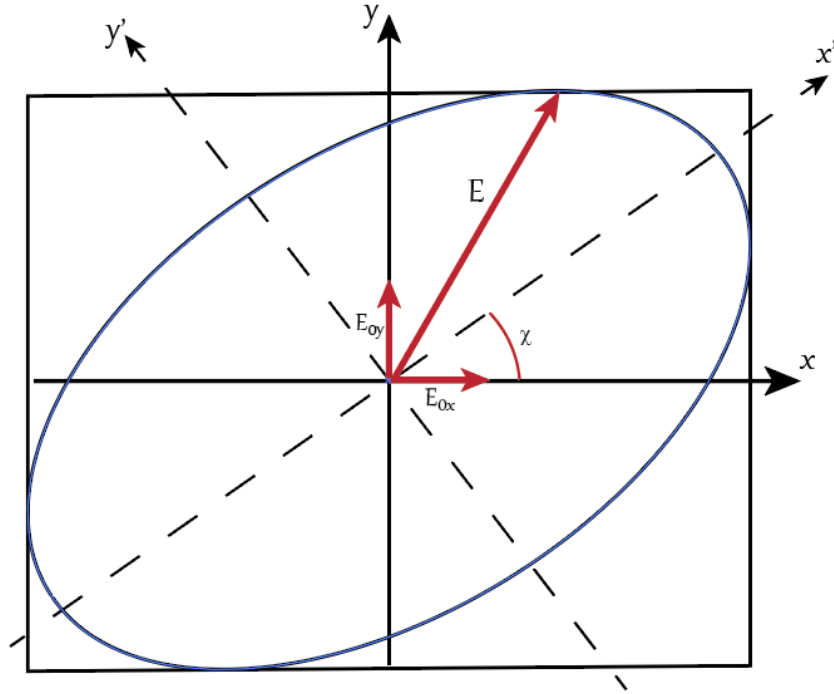


Figure 3.2: Polarization ellipse with electric vector \mathbf{E} showing rotation of x and y electric field components coinciding with the principal axes. Image reproduced from [61].

3.5 Radiative Transfer

3.5.1 Radiative Transfer Equation

The process of radiative transport is dictated by the Boltzmann Transport equation. As a light ray passes through a medium, energy can either be added or subtracted through emission or absorption, forming the basis for radiative transfer. The effects of absorption and emission can be combined into a single radiative transfer equation:

$$\frac{dI_\nu}{ds} = -\alpha_\nu I_\nu + j_\nu, \quad (3.30)$$

where j_ν is the emission coefficient, α_ν is the absorption coefficient, and I_ν is the intensity. This is a useful equation with which to solve for the specific intensity along a ray in an absorbing and emitting medium [61].

The full polarized radiative transfer equation can be written in the form ([15]):

$$\frac{d}{ds} \begin{pmatrix} I' \\ Q' \\ U' \\ V' \end{pmatrix} = \begin{pmatrix} j'_I \\ j'_Q \\ j'_U \\ j'_V \end{pmatrix} - \begin{pmatrix} \chi'_I & \chi'_Q & \chi'_U & \chi'_V \\ \chi'_Q & \chi'_I & \rho'_V & \rho'_U \\ \chi'_U & -\rho'_V & \chi'_I & \rho'_Q \\ \chi'_V & -\rho'_U & -\rho'_Q & \chi'_I \end{pmatrix} \begin{pmatrix} I' \\ Q' \\ U' \\ V' \end{pmatrix}, \quad (3.31)$$

where (I', Q', U', V') are the Stokes parameters, $j'_{I,Q,U,V}$ are the polarized emissivities, $\chi'_{I,Q,U,V}$ are the absorption coefficients, and $\rho'_{V,Q,U}$ represent the one Faraday rotation and two Faraday conversion coefficients, respectively.

3.5.2 Faraday Effects

Faraday effects are a phenomenon where a polarization plane of an electromagnetic wave rotates under the influence of a magnetic field. By this very definition, Faraday effects are a consequence of the polarization coming from strong magnetic fields around BHs, making it an important aspect to understanding JAB systems. From Equation 3.31, the Stokes parameter for linear polarization (V) travels through a magnetized plasma and its electric vector polarization angle (EVPA) is rotated due to Faraday rotation. Faraday conversion exchanges circular and linear polarization therefore interchanging the Stokes parameters of U and V, and results in the direct production of circular polarization.

Faraday rotation is believed to be important for reducing the linear polarization fraction in models of M87 to the observed values. As constrained from the data, SANES have larger Faraday rotation and conversion depths than MADs, mainly due to SANE models requiring larger mass densities to match the observed flux of M87. In addition, SANES also have lower temperatures, which increases the efficiency of Faraday effects.

CHAPTER 4: GRMHD SIMULATIONS

Many early uses of GRMHD simulations were pioneered at the turn of the century [34, 45, 48]. These early developed codes solve the GRMHD equations for a number of quantities, proving relevant to understanding outstanding problems in BH physics. We discuss the GRMHD applications utilized in this work.

4.1 HARM Scheme

The high-accuracy relativistic magnetohydrodynamics (HARM) code created by Gammie, McKinney, and Toth was a foundational piece in developing accurate GRMHD simulations [36]. This conservative, shock-capturing numerical scheme evolves the equations of GRMHD in a new light through the addition of obey shock jump conditions at discontinuities in the fluid variables. The HARM scheme has been used through a variety of applications including investigating radiative models of Sgr A* [53] and simulations of stable relativistic jets [17, 49].

Here, we use two numerical GRMHD simulations. The fluid simulations were produced with KHARMA, a GPU-based descendant of `iharm`. The MHD stress-energy tensor is defined as

$$T^{\mu\nu} = (\rho + u + P + b^2)u^\mu u^\nu + (P + \frac{b^2}{2})g^{\mu\nu} - b^\mu b^\nu, \quad (4.1)$$

where u and P are the internal energy of the fluid and its pressure. These two parameters are related to internal energy via an ideal gas law equation of state consisting of a constant adiabatic index $\hat{\gamma}$ where

$$P = (\hat{\gamma} - 1)u. \quad (4.2)$$

4.2 General Relativistic Radiative Transfer (GRRT)

A proper way to model the accretion disks around BHs is by the use of general relativistic radiative transfer (GRRT) codes. Some of the largely known, open-source codes include GRMONTY [26], GRTRANS [25], IPOLE [51], and KORAL [63]. For our analysis, GRMONTY is used to compute the SED of each source, and IPOLE is used for the production of polarimetric images of the GRMHD simulations employed in this work.

4.2.1 IPOLE

IPOLE is a public ray-tracing code for covariant, polarized radiative transport [51]. It was developed with the goal of generating polarized BH images from EHT's data of Sgr A* and M87. It is a numerical scheme that integrates Equation 3.31 by ray tracing in nontrivial spacetimes as well as in optical and Faraday thick plasmas. It solves for the evolution of the polarized intensities at each point along a geodesic with a two-stage operator splitting method.

IPOLE produces images composing of a $N \times N$ grid with pixels over a $160\mu as$ field of view where each pixel contains each of the four Stokes parameters (I, Q, U, V) . The code evaluates the radiative transfer coefficients in physical units, requiring us to specify the BH size, the mass-density of the accreting plasma, and inclination.

To account for the abnormally high plasma density and temperature caused by IPOLE inability to correctly evolve the fluid state in highly magnetized (R_{low}) regions, a σ cutoff is introduced. The plasma density in those regions with $\sigma > \sigma_{cutoff}$ are set to zero before transfer coefficients are computed.

We add positrons globally in the post-processing in each snapshot of the model. By varying the positron fraction in each frame, we can see how the ratio of electron-positron pair density over electron-ion pair density ($n_{pairs}/(n_-)_0$) goes from $0 \rightarrow 1.0$ affects the polarization across the simulation at specific timesteps.

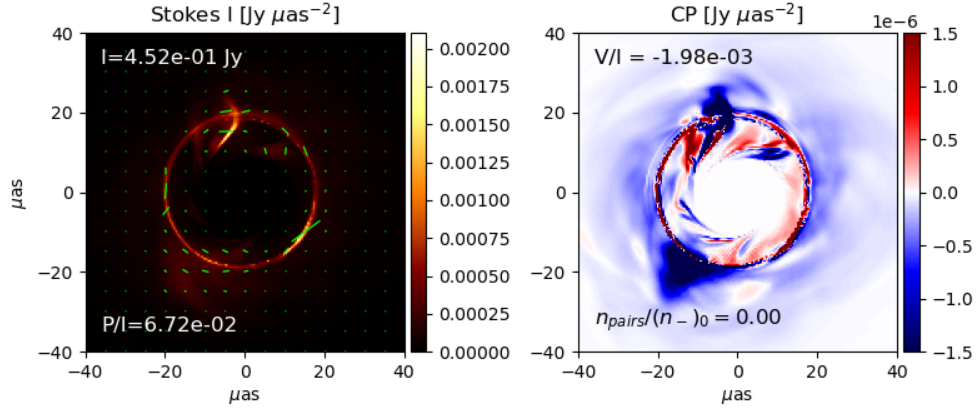


Figure 4.1: An example $R\text{-}\beta$ model of M87 for a MAD at $a = -0.5$ and $T = 30,000M$ for the 230 GHz emission. The left image clearly shows the strong magnetic field with the lack of EVPA. See subsection 4.2.1 for simulation information.

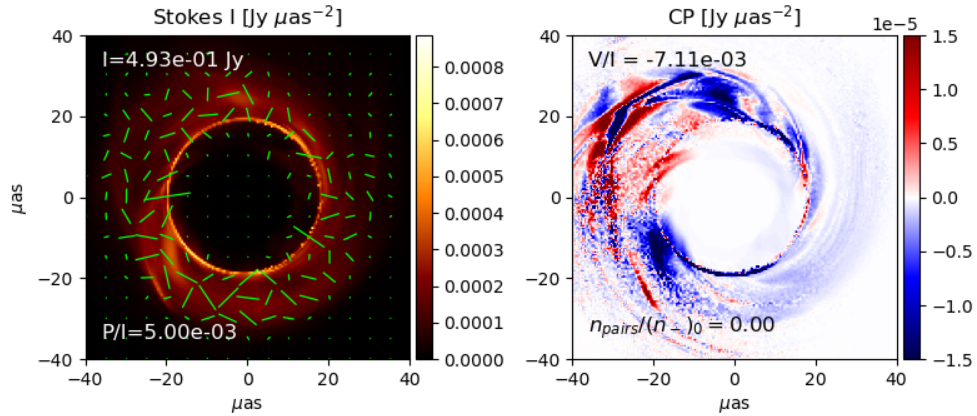


Figure 4.2: An example $R\text{-}\beta$ model of M87 for a SANE at $a = -0.5$ and $T = 30,000M$ for the 230 GHz emission. The larger, chaotic EVPAs in the left image show the characteristic high density of a SANE. See subsection 4.2.1 for simulation information.

4.2.2 GRMONTY

GRMONTY is a Monte Carlo-based radiative transfer code used for calculating spectra of optically thin, ionized plasmas in full GR as tested and described in [26]. This code creates SEDs including the effects of synchrotron emission and self-absorption, bremsstrahlung, and inverse Compton processes with as few approximations as possible, as shown in Figure 4.3. GRMONTY uses a "stationary flow" approximation, computing the SED through each time slice of simulated data as if it were time independent, and the emissivity and absorptivity are constant along any line of sight.

Emission in this code is regarded by sampling the emitted photon field where the samples are called superphotons, or photon packets. The probability distribution for the superphotons is

$$\frac{1}{\sqrt{-g}} \frac{dN_s}{d^3x dt d\nu d\omega} = \frac{1}{\omega \sqrt{-g}} \frac{dN}{d^3x dt d\nu d\omega} = \frac{1}{\omega} \frac{j_\nu}{h\nu}, \quad (4.3)$$

where j_ν is the emissivity and ν is the frequency contained within a solid angle $d\omega$ [26]. Dependence on emissivity is computed only through functions that specify j_ν and $\int d\nu d\omega j_\nu / \nu$.

Absorption is treated deterministically. Scattering in the code consists of two separate parts: 1. Determine where the superphoton should scatter and 2. Determine the energy and direction of said superphoton.

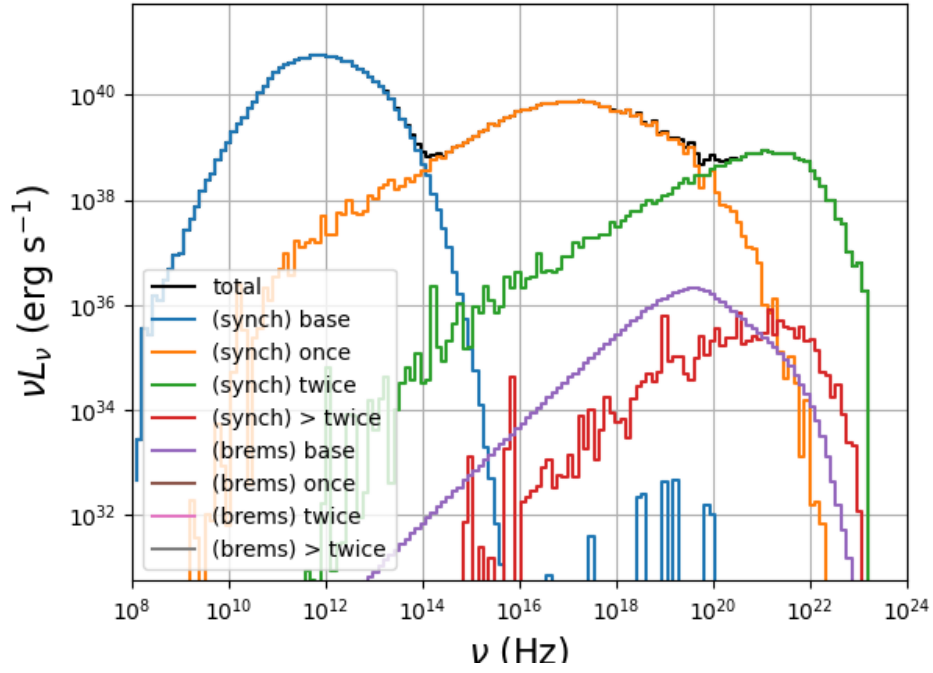


Figure 4.3: An example R - β SED of M87 for a MAD with $a = -0.5$ at $T = 30000M$ for the 230 GHz emission.

CHAPTER 5: EMISSION MODELS

5.1 Turbulent Heating Models

Turbulent heating is the result of dissipation of fluctuations within plasma in these high astrophysical processes and is important to understanding observational evidence [41], especially those from the accretion disk of BHs where temperature can reach exceedingly high temperatures. For a large portion of these plasma environments, the dissipation of these fluctuations occurs at length-scales smaller than the mean free path of the particles, resulting in collisionless plasma.

The question in recent years has been the investigation into differential heating of ions and electrons in turbulent plasma. We describe the two main turbulent heating models used throughout this work.

5.1.1 R- β Model

The R- β turbulent heating model, developed in [52], is the primary model used by the EHT Collaboration:

$$R(\beta) \equiv \frac{T_i}{T_e} = \frac{\beta^2}{1 + \beta^2} R_{high} + \frac{1}{1 + \beta^2} R_{low}. \quad (5.1)$$

Here, $b = \frac{\beta}{\beta_c}$ where β_c is usually assumed to be 1 (consistent with long cooling time of Sgr A*), therefore β is used in the equation for simplicity. T_e depends on the plasma magnetization, T_i comes from the GRMHD simulation, R_{high} defines the electron-to-ion coupling in the weakly magnetized regions or the disk/high β regions, and R_{low} defines the electron-to-ion coupling in the strongly magnetized regions or the jet/low β regions. Dependence on T_i/T_e is mainly due to synchrotron self-absorption, which scales directly with increasing inclination [53].

This model consists of three free parameters: β_c , R_{high} , and R_{low} . Many variations of this parameter space have been tested against EHT constraints [53], [16], [17], [13], [4].

5.1.2 Critical- β Model

Developed in [16], an alternative model to the widely used R- β was introduced:

$$\frac{T_e}{T_e + T_i} = f e^{-\beta/\beta_c} \quad (5.2)$$

where $0 < f < 1$ is a constant. The exponential parameter β_c controls the transition between electron- and ion-dominated heating and is the critical value of β that approximately sets a β_{max} contributing to the observed emission.

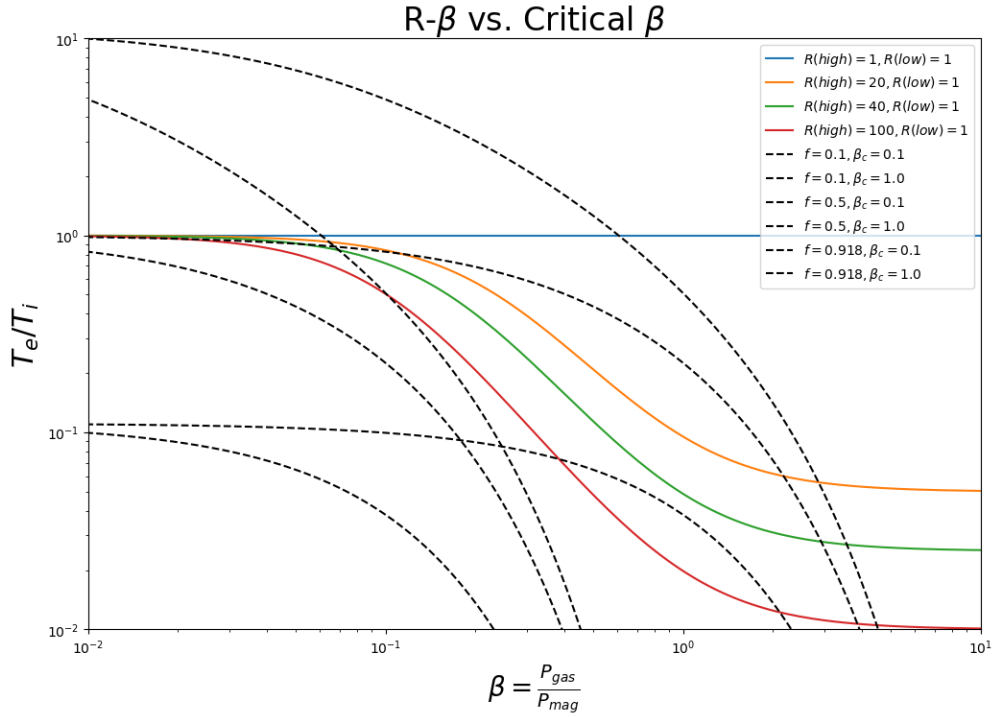


Figure 5.1: Comparison of Critical- β (dashed lines) against R- β (solid lines) for previously tested and reasonable parameters.

The advantage of this model is the ability to probe more intermediate ranges of β between the same temperature range as the R- β model due to the β_{crit} in the exponential [17]. For all values of β_c , the emissions tend to be very concentrated near the corona/interface of the disk and jet. These are areas where the rapidly adiabatic expanding plasma could decrease in temperature as it decreases in radius, making the spectrum steeper than its model counterpart.

Although both models have a similar asymptotic behavior in the low β regime, the Critical- β model exponentially falls to zero at high β as seen in Figure 5.1. Preliminary indications showed this trend may reduce bremsstrahlung contribution [16]. This is a factor that causes R- β to exceed the observational constraints for some of its parameter space due to overproduction of X-rays [4], showing that the Critical- β model may be the more well-suited emission model.

This model includes two free parameters, f and β_c , which have only been tested for the following values:

Target	f	β_c	Reference
Sgr A*	0.1	0.01	[16]
Sgr A*	0.1	0.1	[16]
Sgr A*	0.1	1.0	[16]
Sgr A*	0.5	0.01	[16]
Sgr A*	0.5	0.1	[16]
Sgr A*	0.5	1.0	[16]
Sgr A*	0.5	1.0	[4]
M87	0.5	1.0	[17]

Table 5.1: Previously tested (f, β_c) values where most of the Sag A* investigation comes from the initial introduction of the Critical- β Model in Anantua et. al [16].

Table 5.1 has only been tested for Sgr A* besides one parameter set in [17] for the purpose of modeling the JAB system of M87. EHT has yet to test the Critical- β model for M87.

5.1.3 Alternative Models: Magnetic Reconnection and Shocks

Constant Electron Beta Model

When the electron energy density (u_e) is held constant as a fraction of the magnetic energy density (u_B), the Constant Electron Beta Model or Constant β_e Model is described through the relation $\beta_e = P_e/P_B = (\gamma_e - 1)u_e/(b^2/2) = \beta_{e0}$ or more conveniently

$$P_e = \beta_{e0}P_B \tag{5.3}$$

where $b^2 = b^\mu b_\mu$. This model is only parameterized by one free parameter: β_{e0} and is a relatively simple prescription for linking plasma variables to radiation by describing a region of force-free, relativistic plasma. This model becomes viable when magnetic reconnection is the dominant source for the heating of electrons, as is thought to be in the jet regions of JAB systems [16]. It is utilized in our polarimetric images to construct M87 with the inclusion of a jet.

New Model with Shock Inclusion

As magnetic fields play a critical role in the morphology of JAB systems, a model with the inclusion of shockwaves would be beneficial to the library of emission processes. We propose a much-needed analytical model to capture the shock region causing dissipation of energy into radiating particles, an emission mechanism not yet fully considered in JAB systems.

To quantify the shocks within the jet, we propose a model consisting of a fraction of the internal energy (U) described by a new parameter η simply parameterized as:

$$P_e = \eta U. \tag{5.4}$$

This model is analogous to the Constant β_e Jet Model that we intend to implement in our simulations as part of the future directions.

5.2 Parameter Space for Investigation

Since the mass accretion rate within our code is an adjustable parameter with which the flux scales, all models are scaled so that the 230 GHz flux density is 0.5 Jy for synthetic images. To scale our dimensionless GRMHD simulations with the BH mass accretion rate (\dot{M}), we require a dimensionless mass unit (\mathcal{M}) for each of our models. We investigate two different dimensionless BH spins $a_* = -0.5$ and $+0.94$. We observe our simulations at one inclination angle $i = 163^\circ$. In addition, we focus on the time evolution through three specific time steps for each model: 20,000, 25,000, and 30,000 GM_{M87}/c^3 . The GRMHD snapshots were evolved for $10,000 GM_{M87}/c^3$ time units.

This corresponds to ≈ 10 years. We define a jet in the model when a transitional value of $\sigma = 0.5$ is used within IPOLE.

5.2.1 R- β Parameters

Table 5.2 displays the R- β values investigated. Although already thoroughly tested throughout EHT collaborator papers [7, 17, 52], we aim to use this parameter set as a comparison.

R- β Parameters					
Mode	i [°]	a_*	R_{high}	R_{low}	β_c
MAD	163°	-0.5	20	1	1
MAD	163°	+0.94	20	1	1
SANE	163°	-0.5	20	1	1
SANE	163°	+0.94	20	1	1

Table 5.2: Values for free parameters in R- β model for all three timesteps. β_c is a constant always to be used as a value of 1.

The temperature ratio (T_i/T_e) can be used as a free parameter and specified as done in other investigations ([53]). Within our simulations, we take T_i/T_e to be a mixed and randomized ratio for the R- β model. This is to ensure the focus on the free parameters listed in Table 5.2 only.

5.2.2 Critical- β Parameters

We expand the Critical- β parameter space by testing value sets for M87 for the first time. The values listed in Table 5.3 describe the space to be investigated.

Critical- β Parameters				
Mode	i [°]	a_*	f	β_c
MAD	163°	-0.5	0.5	1.0
MAD	163°	+0.94	0.5	1.0
SANE	163°	-0.5	0.5	1.0
SANE	163°	+0.94	0.5	1.0
MAD	163°	-0.5	0.5	0.1
MAD	163°	+0.94	0.5	0.1

Table 5.3: Values tested for free parameters in Critical- β model for all three timesteps.

As explicitly stated for R- β , the temperature ratio ($T_e/T_e + T_i$) is mixed and randomized within

the simulations. This is to ensure the focus on the free parameters listed in Table 5.3 only. As $f = 0.5$ is the more widely tested parameter within the model, we use that as a constant and vary β_c for this investigation.

5.3 Positron Effects

Although most GRMHD simulations consider a standard electron-ion dominated plasma, it is still unknown whether the plasma in accretion disks is electron-ion dominated or electron-positron pair dominated. As an often overlooked feature in modeling, we investigate how the morphology of simulation is affected by the inclusion of electron-positron pair plasma.

In the JAB systems we consider, the electron-positron pairs are mainly produced through the Breit-Wheeler process which describes pair production as a result of photon-photon collision [20]. The center of momentum energy of the photon-photon collision needs to exceed the rest-mass energy of a pair ($1 \text{ MeV} \approx 2 \times (1.2 \times 10^{20}) \text{ Hz}$).

As GRMONTY currently does not have the modifications necessary to model electron-positron pair dominated plasma, we compare the morphology of the models through our polarimetric images without the assistance of the SEDs.

CHAPTER 6: RESULTS AND MODEL COMPARISONS

6.1 Comparison of Simulations with Observations

6.1.1 Comparison with Polarization Constraints

For an accurate representation of our fiducial models, we compare our linear and circular polarization values against EHT observed constraints. The linear polarization is summed from net (unresolved) Q , U , and I across the image plane,

$$|m|_{net} = \frac{\sqrt{(\sum_i Q_i)^2 + (\sum_i U_i)^2}}{\sum_i I_i} \quad (6.1)$$

as well as its average local (resolved) magnitude

$$\langle |m| \rangle = \frac{\sum_i I_i P_i}{\sum_i I_i} = \frac{\sum_i \sqrt{Q_i^2 + U_i^2}}{\sum_i I_i}. \quad (6.2)$$

In an analogous manner, the resolved circular polarization can be quantified as

$$\langle |V| \rangle = \frac{\int |V/I| I dA}{\int I dA}, \quad (6.3)$$

where I is the Stokes intensity and $|V/I|$ is the image-averaged fractional circular polarization magnitude [5]. The unresolved magnitude is found to be

$$V_{net} = \frac{\int V dA}{\int I dA}. \quad (6.4)$$

Tables 6.1 and 6.2 show the median values for circular and linear polarization for all three timesteps, respectively. We see an overwhelming rate of both models passing the circular polarization constraints, yet only a handful passing for the median linear polarization constraints. For full polarization tables for individual timesteps, see Appendix A.

	$R-\beta$	SANE $R-\beta$ w./ Jet	($a = -0.5$) Crit - β w./ Jet	Crit - β w./ Jet	$R-\beta$	MAD $R-\beta$ w./ Jet	($a = -0.5$) Crit - β w./ Jet	Crit - β w./ Jet
$ V _{net}(f_{pos,min})$	$-5.60 \cdot 10^{-3}$	$-1.68 \cdot 10^{-3}$	$-2.17 \cdot 10^{-3}$	$5.48 \cdot 10^{-3}$	$-4.48 \cdot 10^{-3}$	$-3.53 \cdot 10^{-3}$	$-3.58 \cdot 10^{-3}$	$-3.02 \cdot 10^{-3}$
$ V _{net}(f_{pos,max})$	$1.04 \cdot 10^{-2}$	$2.59 \cdot 10^{-3}$	$5.52 \cdot 10^{-2}$	$1.04 \cdot 10^{-2}$	$-2.09 \cdot 10^{-3}$	$-9.43 \cdot 10^{-4}$	$-1.67 \cdot 10^{-3}$	$-1.03 \cdot 10^{-3}$
$\langle V \rangle (f_{pos,min})$	$8.39 \cdot 10^{-3}$	$4.94 \cdot 10^{-3}$	$1.27 \cdot 10^{-2}$	$7.34 \cdot 10^{-3}$	$3.60 \cdot 10^{-3}$	$2.76 \cdot 10^{-3}$	$3.27 \cdot 10^{-3}$	$2.56 \cdot 10^{-3}$
$\langle V \rangle (f_{pos,max})$	$1.28 \cdot 10^{-2}$	$6.41 \cdot 10^{-3}$	$2.63 \cdot 10^{-2}$	$1.15 \cdot 10^{-2}$	$9.32 \cdot 10^{-4}$	$5.75 \cdot 10^{-4}$	$8.57 \cdot 10^{-4}$	$5.66 \cdot 10^{-4}$
	$R-\beta$	SANE $R-\beta$ w./ Jet	($a = +0.94$) Crit - β w./ Jet	Crit - β w./ Jet	$R-\beta$	MAD $R-\beta$ w./ Jet	($a = +0.94$) Crit - β w./ Jet	Crit - β w./ Jet
$ V _{net}(f_{pos,min})$	$2.12 \cdot 10^{-2}$	$4.06 \cdot 10^{-2}$	$1.20 \cdot 10^{-3}$	$-3.91 \cdot 10^{-4}$	$-1.68 \cdot 10^{-3}$	$-1.71 \cdot 10^{-3}$	$-2.16 \cdot 10^{-3}$	$-1.90 \cdot 10^{-3}$
$ V _{net}(f_{pos,max})$	$2.93 \cdot 10^{-2}$	$4.84 \cdot 10^{-2}$	$5.71 \cdot 10^{-3}$	$6.27 \cdot 10^{-3}$	$-1.30 \cdot 10^{-4}$	$-3.63 \cdot 10^{-4}$	$-4.54 \cdot 10^{-4}$	$-4.60 \cdot 10^{-4}$
$\langle V \rangle (f_{pos,min})$	$6.65 \cdot 10^{-3}$	$1.20 \cdot 10^{-2}$	$8.97 \cdot 10^{-3}$	$1.62 \cdot 10^{-2}$	$2.91 \cdot 10^{-3}$	$2.08 \cdot 10^{-3}$	$2.90 \cdot 10^{-3}$	$2.14 \cdot 10^{-3}$
$\langle V \rangle (f_{pos,max})$	$1.52 \cdot 10^{-2}$	$2.62 \cdot 10^{-2}$	$6.48 \cdot 10^{-3}$	$1.41 \cdot 10^{-2}$	$6.85 \cdot 10^{-4}$	$3.65 \cdot 10^{-4}$	$6.51 \cdot 10^{-4}$	$3.94 \cdot 10^{-4}$

Table 6.1: Median circular polarization for $|V|_{net}$ and $\langle |V| \rangle$ for $20,000M - 30,000M$. The bold models satisfy the EHT limit of $-8.0 \cdot 10^{-3} V_{net} < 8.0 \cdot 10^{-3}$ and $0 < \langle |V| \rangle < 3.7 \cdot 10^{-2}$.

	$R-\beta$	SANE $R-\beta$ w./ Jet	($a = -0.5$) Crit - β w./ Jet	Crit - β w./ Jet	$R-\beta$	MAD $R-\beta$ w./ Jet	($a = -0.5$) Crit - β w./ Jet	Crit - β w./ Jet
$ m _{net}(f_{pos,min})$	$5.00 \cdot 10^{-3}$	$4.96 \cdot 10^{-3}$	$2.25 \cdot 10^{-3}$	$5.69 \cdot 10^{-3}$	$6.72 \cdot 10^{-2}$	$4.34 \cdot 10^{-2}$	$6.49 \cdot 10^{-2}$	$4.63 \cdot 10^{-2}$
$ m _{net}(f_{pos,max})$	$5.37 \cdot 10^{-3}$	$6.30 \cdot 10^{-3}$	$2.73 \cdot 10^{-3}$	$6.14 \cdot 10^{-3}$	$5.52 \cdot 10^{-2}$	$3.10 \cdot 10^{-2}$	$5.68 \cdot 10^{-2}$	$3.53 \cdot 10^{-2}$
$\langle m \rangle_{net}(f_{pos,min})$	$1.39 \cdot 10^{-1}$	$1.42 \cdot 10^{-1}$	$1.35 \cdot 10^{-1}$	$1.46 \cdot 10^{-1}$	$3.49 \cdot 10^{-1}$	$3.24 \cdot 10^{-1}$	$2.71 \cdot 10^{-1}$	$2.61 \cdot 10^{-1}$
$\langle m \rangle_{net}(f_{pos,max})$	$1.31 \cdot 10^{-1}$	$1.48 \cdot 10^{-1}$	$1.39 \cdot 10^{-1}$	$1.50 \cdot 10^{-1}$	$4.63 \cdot 10^{-1}$	$4.15 \cdot 10^{-1}$	$4.02 \cdot 10^{-1}$	$3.91 \cdot 10^{-1}$
	$R-\beta$	SANE $R-\beta$ w./ Jet	($a = +0.94$) Crit - β w./ Jet	Crit - β w./ Jet	$R-\beta$	MAD $R-\beta$ w./ Jet	($a = +0.94$) Crit - β w./ Jet	Crit - β w./ Jet
$ m _{net}(f_{pos,min})$	$1.37 \cdot 10^{-2}$	$1.41 \cdot 10^{-2}$	$1.64 \cdot 10^{-2}$	$1.18 \cdot 10^{-2}$	$4.91 \cdot 10^{-2}$	$4.56 \cdot 10^{-2}$	$3.07 \cdot 10^{-2}$	$3.67 \cdot 10^{-2}$
$ m _{net}(f_{pos,max})$	$2.55 \cdot 10^{-2}$	$2.25 \cdot 10^{-2}$	$9.03 \cdot 10^{-3}$	$8.76 \cdot 10^{-3}$	$5.17 \cdot 10^{-2}$	$5.01 \cdot 10^{-2}$	$4.38 \cdot 10^{-2}$	$4.82 \cdot 10^{-2}$
$\langle m \rangle_{net}(f_{pos,min})$	$1.29 \cdot 10^{-1}$	$2.58 \cdot 10^{-1}$	$2.17 \cdot 10^{-1}$	$2.24 \cdot 10^{-1}$	$5.76 \cdot 10^{-1}$	$5.22 \cdot 10^{-1}$	$5.06 \cdot 10^{-1}$	$4.88 \cdot 10^{-1}$
$\langle m \rangle_{net}(f_{pos,max})$	$2.22 \cdot 10^{-1}$	$2.65 \cdot 10^{-1}$	$2.16 \cdot 10^{-1}$	$2.31 \cdot 10^{-1}$	$5.86 \cdot 10^{-1}$	$5.32 \cdot 10^{-1}$	$5.76 \cdot 10^{-1}$	$5.27 \cdot 10^{-1}$

Table 6.2: Median linear polarization for $|m_{net}|$ and $\langle |m| \rangle$. From [8], observational constraints were found to be $0.01 \leq |m_{net}| \leq 0.037$ and $0.057 < \langle |m| \rangle < 0.107$. The bold values refer to values that satisfy the linear polarization constraints.

6.1.2 Comparison with β_2

Palumbo et al. [56] discovered the B-field in simulated accretion flows of M87 was encoded in the morphology of the EVPAs at 230 GHz, showing circular EVPAs corresponding to MADs and more radially EVPAs corresponding to SANEs. An azimuthal decomposition was proposed to differentiate between the two accretion flows in a polarized image using the equation:

$$\beta_m = \frac{1}{I_{total}} \int_0^{+\infty} \int_0^{2\pi} P(\rho, \varphi) e^{-im\varphi} \rho d\varphi d\rho, \quad (6.5)$$

where φ is the image azimuthal angle when averaged over image radius ρ , I_{total} is the intensity, and $P = Q + iU$ describes the linear polarization referring to both Stokes parameters.

The $m = 2$ mode is rotationally symmetric and therefore produces a nearly rotationally symmetric image when viewed face-on. This is important as this is the case for M87, leading us to investigate only the β_2 mode, as it is the most informative to distinguish between the two accretion states.

Tables 6.3, 6.4, and 6.5 show the β_2 values for all three timesteps for the standard parameter space we observe for both R- β ($R_{low} = 1, R_{high} = 20$) and Critical- β ($f = 0.5, \beta_c = 1.0$). Using EHT's constraint from [8], bold values in the tables below mark models that fit between the $0.04 < \beta_2 < 0.7$ constraint. No fiducial models for SANEs pass the β_2 constraint, while few MAD models pass.

	SANE ($a = -0.5$)				MAD ($a = -0.5$)			
$R-\beta$	$R-\beta$	Crit - β	Crit - β	$R-\beta$	$R-\beta$	Crit - β	Crit - β	
	w./ Jet		w./ Jet		w./ Jet		w./ Jet	
$\beta_2(f_{pos,min})$	$2.96 \cdot 10^{-3}$	$1.38 \cdot 10^{-3}$	$1.64 \cdot 10^{-3}$	$1.40 \cdot 10^{-3}$	$7.55 \cdot 10^{-2}$	$1.10 \cdot 10^{-1}$	$7.57 \cdot 10^{-2}$	$1.03 \cdot 10^{-1}$
$\beta_2(f_{pos,max})$	$7.20 \cdot 10^{-4}$	$2.72 \cdot 10^{-3}$	$2.07 \cdot 10^{-3}$	$4.25 \cdot 10^{-3}$	$7.09 \cdot 10^{-2}$	$4.06 \cdot 10^{-2}$	$8.78 \cdot 10^{-2}$	$1.24 \cdot 10^{-1}$
	SANE ($a = +0.94$)				MAD ($a = +0.94$)			
$R-\beta$	$R-\beta$	Crit - β	Crit - β	$R-\beta$	$R-\beta$	Crit - β	Crit - β	
	w./ Jet		w./ Jet	w./ Jet	w./ Jet		w./ Jet	
$\beta_2(f_{pos,min})$	$5.72 \cdot 10^{-3}$	$1.99 \cdot 10^{-3}$	$8.93 \cdot 10^{-4}$	$5.00 \cdot 10^{-3}$	$3.26 \cdot 10^{-2}$	$2.93 \cdot 10^{-2}$	$3.04 \cdot 10^{-2}$	$2.90 \cdot 10^{-2}$
$\beta_2(f_{pos,max})$	$1.24 \cdot 10^{-2}$	$5.12 \cdot 10^{-3}$	$1.17 \cdot 10^{-2}$	$9.18 \cdot 10^{-3}$	$3.31 \cdot 10^{-2}$	$2.87 \cdot 10^{-2}$	$3.49 \cdot 10^{-2}$	$3.08 \cdot 10^{-2}$

Table 6.3: Azimuthal structure mode β_2 for fiducial models at $T = 20,000M$. The observational constraints from EHT M87 Paper VII are in the range $0.04 \leq |\beta_2| \leq 0.07$. The bold value refers to the fiducial model which satisfies the observational constraints.

	SANE ($a = -0.5$)				MAD ($a = -0.5$)			
$R-\beta$	$R-\beta$	Crit - β	Crit - β	$R-\beta$	$R-\beta$	Crit - β	Crit - β	
	w./ Jet		w./ Jet		w./ Jet		w./ Jet	
$\beta_2(f_{pos,min})$	$3.51 \cdot 10^{-3}$	$2.82 \cdot 10^{-3}$	$3.84 \cdot 10^{-3}$	$3.80 \cdot 10^{-3}$	$6.22 \cdot 10^{-3}$	$6.31 \cdot 10^{-3}$	$1.17 \cdot 10^{-2}$	$6.18 \cdot 10^{-3}$
$\beta_2(f_{pos,max})$	$2.96 \cdot 10^{-3}$	$3.03 \cdot 10^{-3}$	$4.24 \cdot 10^{-3}$	$9.86 \cdot 10^{-4}$	$1.47 \cdot 10^{-2}$	$9.83 \cdot 10^{-3}$	$2.15 \cdot 10^{-2}$	$1.32 \cdot 10^{-2}$
	SANE ($a = +0.94$)				MAD ($a = +0.94$)			
$R-\beta$	$R-\beta$	Crit - β	Crit - β	$R-\beta$	$R-\beta$	Crit - β	Crit - β	
	w./ Jet		w./ Jet	w./ Jet	w./ Jet		w./ Jet	
$\beta_2(f_{pos,min})$	$2.25 \cdot 10^{-2}$	$7.28 \cdot 10^{-3}$	$5.54 \cdot 10^{-3}$	$7.69 \cdot 10^{-3}$	$3.23 \cdot 10^{-2}$	$2.42 \cdot 10^{-2}$	$3.58 \cdot 10^{-2}$	$2.77 \cdot 10^{-2}$
$\beta_2(f_{pos,max})$	$2.85 \cdot 10^{-2}$	$1.11 \cdot 10^{-2}$	$1.15 \cdot 10^{-2}$	$5.01 \cdot 10^{-3}$	$3.93 \cdot 10^{-2}$	$2.72 \cdot 10^{-2}$	$3.55 \cdot 10^{-2}$	$2.72 \cdot 10^{-2}$

Table 6.4: Azimuthal structure mode β_2 for fiducial models at $T = 25,000M$. The observational constraints from EHT M87 Paper VII are in the range $0.04 \leq |\beta_2| \leq 0.07$. The bold values refer to fiducial models which satisfy the observational constraints.

	SANE ($a = -0.5$)				MAD ($a = -0.5$)			
	$R-\beta$	$R-\beta$	Crit $-\beta$	Crit $-\beta$	$R-\beta$	$R-\beta$	Crit $-\beta$	Crit $-\beta$
	w./ Jet		w./ Jet		w./ Jet		w./ Jet	
$\beta_2(f_{\text{pos,min}})$	$5.54 \cdot 10^{-3}$	$8.34 \cdot 10^{-3}$	$2.43 \cdot 10^{-3}$	$4.02 \cdot 10^{-3}$	$3.96 \cdot 10^{-2}$	$3.36 \cdot 10^{-2}$	$2.68 \cdot 10^{-2}$	$3.94 \cdot 10^{-2}$
$\beta_2(f_{\text{pos,max}})$	$3.99 \cdot 10^{-4}$	$8.63 \cdot 10^{-3}$	$1.50 \cdot 10^{-3}$	$3.57 \cdot 10^{-3}$	$3.77 \cdot 10^{-2}$	$3.34 \cdot 10^{-2}$	$3.61 \cdot 10^{-2}$	$6.65 \cdot 10^{-2}$
	SANE ($a = +0.94$)				MAD ($a = +0.94$)			
	$R-\beta$	$R-\beta$	Crit $-\beta$	Crit $-\beta$	$R-\beta$	$R-\beta$	Crit $-\beta$	Crit $-\beta$
	w./ Jet		w./ Jet		w./ Jet		w./ Jet	
$\beta_2(f_{\text{pos,min}})$	$1.04 \cdot 10^{-2}$	$7.49 \cdot 10^{-3}$	$7.02 \cdot 10^{-3}$	$5.10 \cdot 10^{-3}$	$2.69 \cdot 10^{-2}$	$1.85 \cdot 10^{-2}$	$1.00 \cdot 10^{-2}$	$3.76 \cdot 10^{-3}$
$\beta_2(f_{\text{pos,max}})$	$9.70 \cdot 10^{-3}$	$1.40 \cdot 10^{-2}$	$5.76 \cdot 10^{-3}$	$2.19 \cdot 10^{-2}$	$3.51 \cdot 10^{-2}$	$1.93 \cdot 10^{-2}$	$1.28 \cdot 10^{-2}$	$9.57 \cdot 10^{-3}$

Table 6.5: Azimuthal structure mode β_2 for fiducial models at $T = 30,000M$. The observational constraints from EHT M87 Paper VII are in the range $0.04 \leq |\beta_2| \leq 0.07$. The bold value refers to the fiducial model which satisfies the observational constraints.

6.2 Bremsstrahlung Contribution

We investigate the contribution of bremsstrahlung radiation in the JAB system as a way to compare the reliability of the models. Following the results of EHT’s work over Sgr A*, some of the $R-\beta$ models failed observational constraints due to overproduction of X-rays from excess bremsstrahlung [4]. While preliminary results in [17] indicated the Critical- β model may reduce this excess bremsstrahlung, we discuss our full results following that investigation here.

6.2.1 MAD Effects

Figures 6.1 and 6.2 show a direct comparison of spectra for the standard parameter set of $R-\beta$ ($R_{\text{low}} = 1, R_{\text{high}} = 2$) and Critical- β ($f = 0.5, \beta_c = 1.0$) for a single snapshot. For MAD $a = -0.5$ there is a consistent and obvious lower contribution of bremsstrahlung from the Critical- β model through all timesteps. For MAD $a = +0.94$, although not obvious, the bremsstrahlung line is overall lower for Critical- β across all timesteps compared to $R-\beta$.

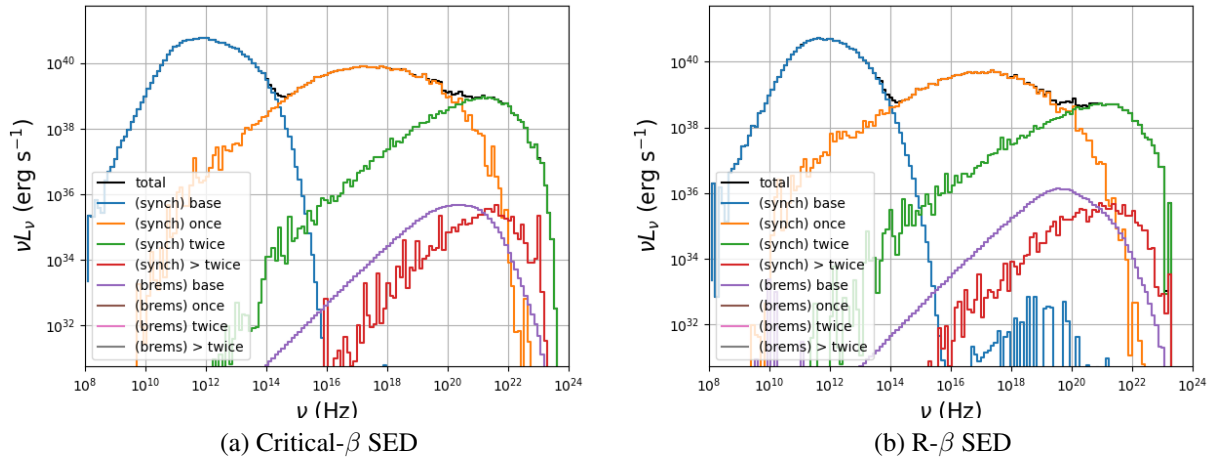


Figure 6.1: Spectra for MAD $a = -0.5$ and $T = 20,000M$. Left: SED for the Critical- β model showing lower bremsstrahlung contribution (purple) contributing to the validity of the model where $f = 0.5$ and $\beta_c = 1$. Right: SED for the R- β model where bremsstrahlung surpasses 10^{36} erg s^{-1} . R_{low} is the standard 1 and $R_{high} = 20$.

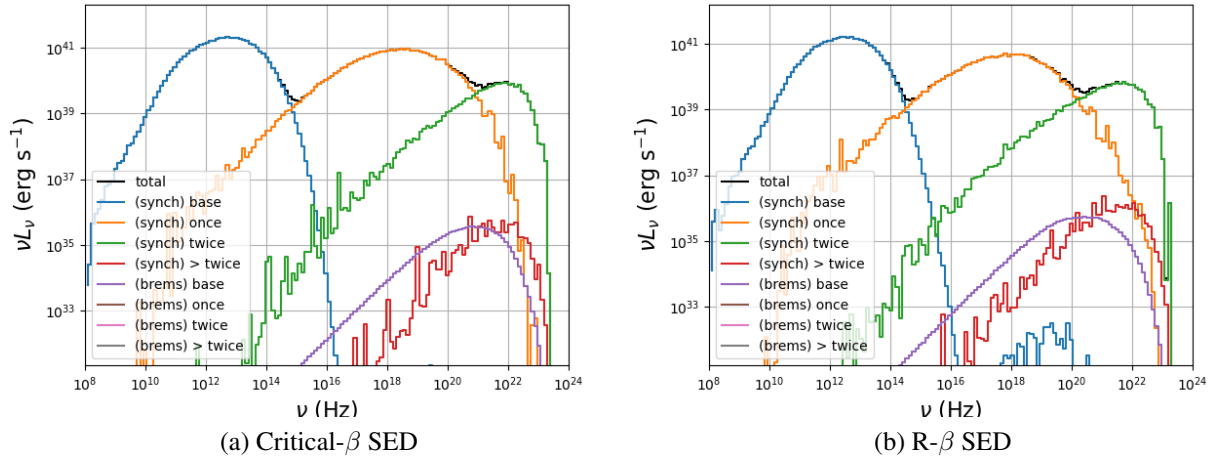


Figure 6.2: Spectra for MAD $a = +0.94$ and $T = 25,000M$. Left: SED for the Critical- β model showing slightly lower bremsstrahlung contribution (purple) contributing to the validity of the model where $f = 0.5$ and $\beta_c = 1$. Right: SED for the R- β model where R_{low} is the standard 1 and $R_{high} = 20$.

In investigating how the effects are changed using the lower β_c values listed in Table 5.3, we observe even lower bremsstrahlung peaks in two different spins in Figure 6.3 than in previously computed Critical- β SEDs.

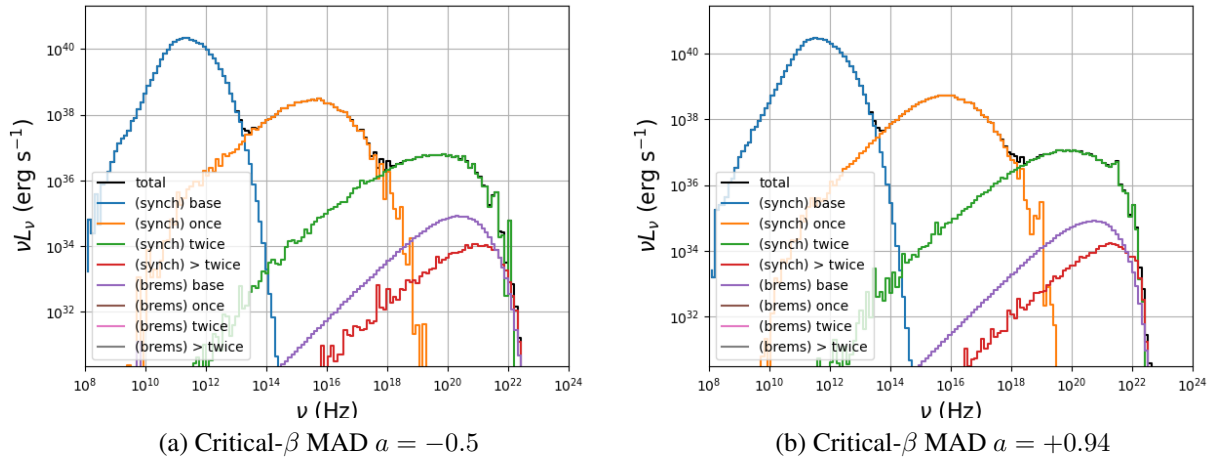


Figure 6.3: Spectra for MAD Critical- β at two different spins for $T = 20,000M$. SED is computed using the values $f = 0.5$ and $\beta_c = 0.1$. We observe once the β_c value is lowered from the standard 1.0, the bremsstrahlung contribution (purple) is one magnitude lower than its previous Critical- β model counterparts.

6.2.2 SANE Effects

Figures 6.4 and 6.5 show a direct comparison of spectra for the standard parameter set of R- β ($R_{low} = 1, R_{high} = 2$) and Critical- β ($f = 0.5, \beta_c = 1.0$) for a single snapshot. The SANEs have a more prominent bremsstrahlung contribution in all our models when compared against MADs. For both SANE spins ($a = -0.5, +0.94$), there is a large distinction between bremsstrahlung contribution between both R- β and Critical- β . The Critical- β model has up to orders of six magnitude less bremsstrahlung radiation.

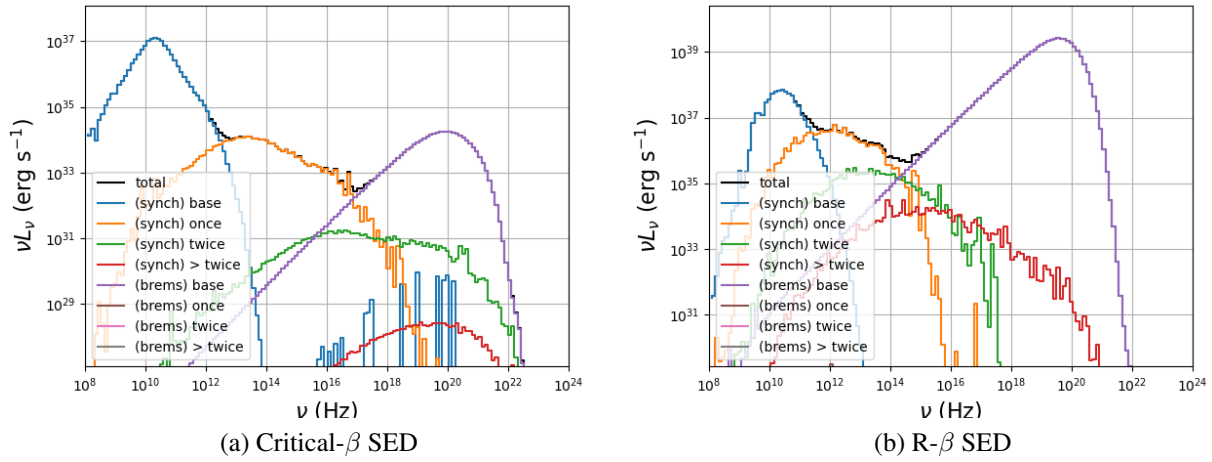


Figure 6.4: Spectra for SANE $a = -0.5$ and $T = 30,000M$. Left: SED for the Critical- β model showing extremely lower bremsstrahlung contribution (purple) where $f = 0.5$ and $\beta_c = 1$. Right: SED for the R- β model where bremsstrahlung surpasses 10^{39} erg s⁻¹ showing a magnitude of 6 difference. R_{low} is the standard 1 and $R_{high} = 20$.

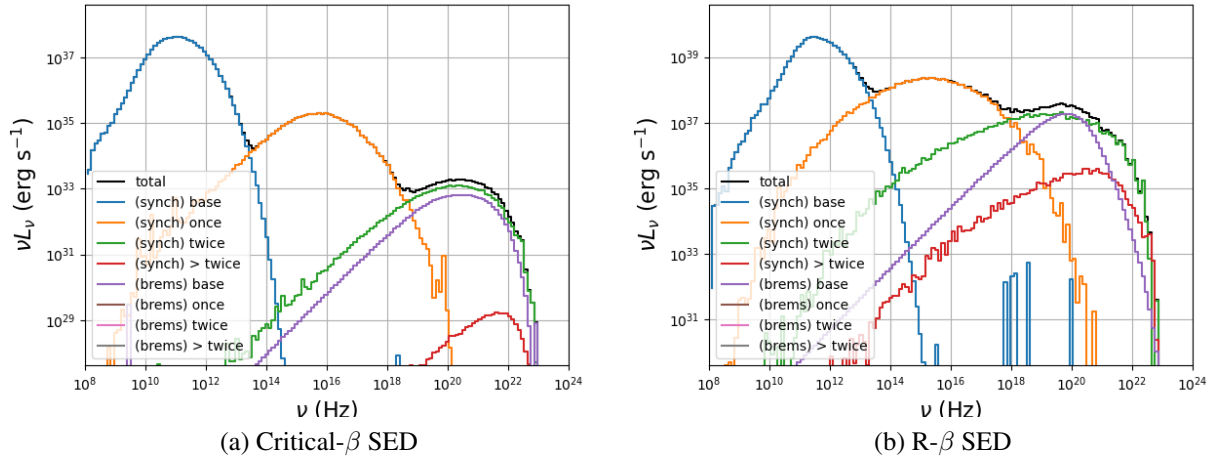


Figure 6.5: Spectra for SANE $a = +0.94$ and $T = 30,000M$. Left: SED for the Critical- β model showing extremely lower bremsstrahlung contribution (purple) where $f = 0.5$ and $\beta_c = 1$. Right: SED for the R- β model where bremsstrahlung surpasses 10^{37} erg s⁻¹ showing a magnitude of 4 difference. R_{low} is the standard 1 and $R_{high} = 20$.

We note inconsistencies with matching observational data at the 230 GHz line or between $10^{11} - 10^{12}$ Hz for our SANE models due to our current dimensionless mass unit (\mathcal{M}) within our simulations. Despite this, we notice the trend of bremsstrahlung > in the R- β model of Figure 6.4

greatly exceeds SED trends throughout the literature [27, 31, 68] even when scaled correctly.

6.3 Flux Eruption Events

As we study the temporal variation in the GRMHD simulation, there are noticeable flux eruption events at certain snapshots shown in Figure 6.6. M87 has been observed to have noticeable variability in both intensity and polarization morphology over a timescale of thousands of gravitational radii (years) [66].

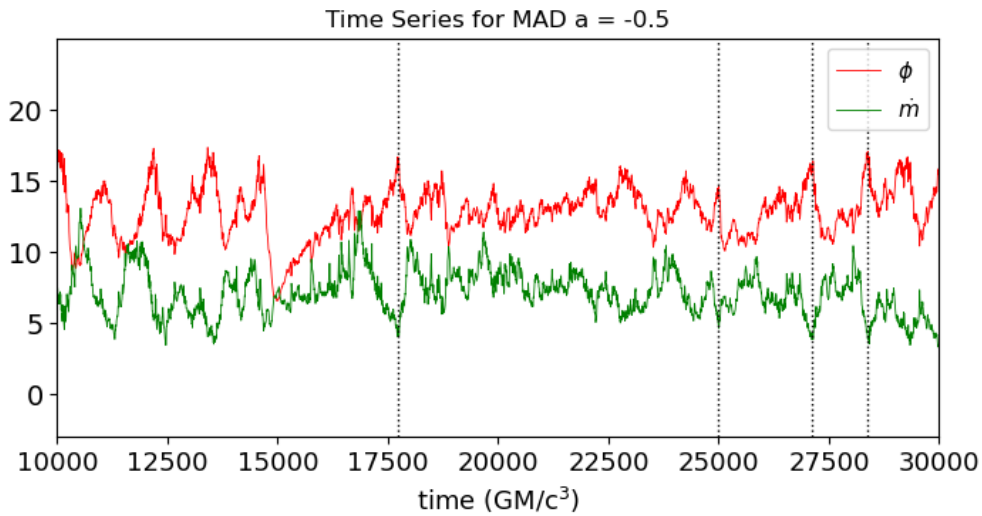


Figure 6.6: Temporal evolution of the MAD $a = -0.5$ simulation with horizon threading flux ϕ (red) and mass accretion rate \dot{m} (green) for $T = 10,000M - 30,000M$. The vertical dotted lines at $T = 17,730M$, $25,000M$, and $27,110M$ show the sharp peaks in ϕ with the troughs in \dot{m} showing the flux eruption events for those individual timestamps.

At $T = 25,000M$ for a MAD $a = -0.5$ displayed in Figure 6.7, there is a large visible flux loop suggesting there may be a broader episodic phenomenon occurring throughout the evolution of the accretion flow, as the flux loop is less noticeable at both individual timesteps before ($20,000M$) and after ($30,000M$). Similar loop structures were observed for $T = 17,730$ and $T = 27,110M$ with similar peaks and troughs for ϕ and \dot{m} , respectively. This sharp rise in the horizon threading flux, accompanied by a sharp decrease in the mass accretion rate, is in accordance with the flux eruption scenario in which a highly polarized magnetic flux loop is added to a MAD.

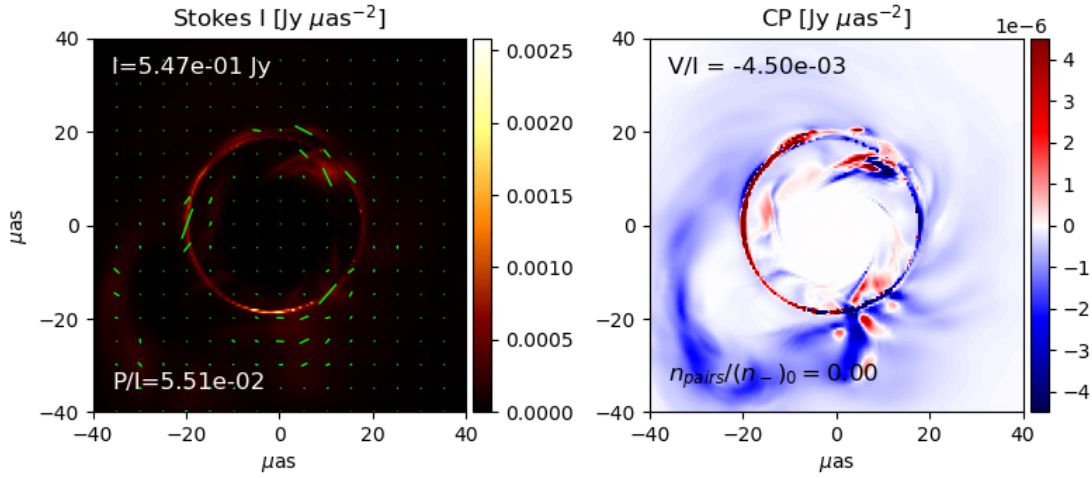


Figure 6.7: For $R\text{-}\beta a = -0.5$ MAD at $T = 25,000M$, there is a noticeable flux eruption loop outside of the photon ring in the circular polarization image on the right.

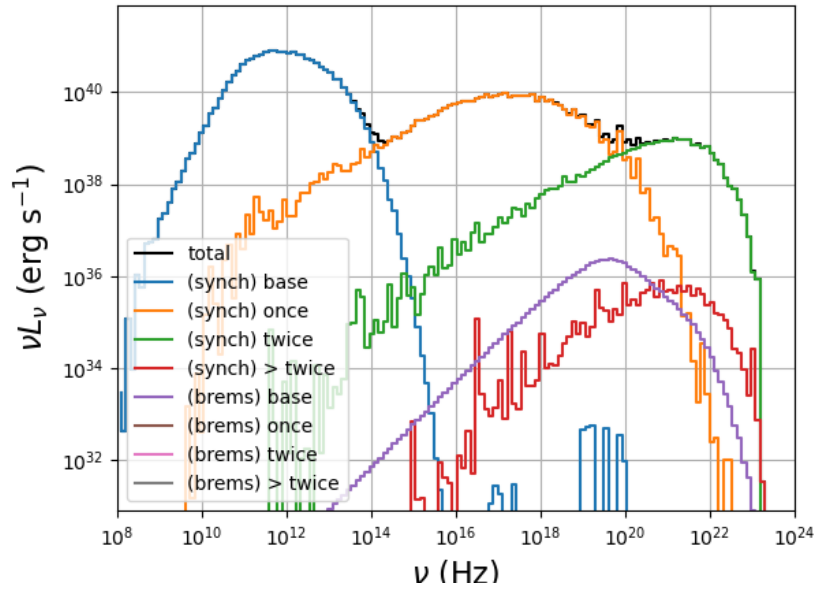


Figure 6.8: Accompanying spectra for $R\text{-}\beta a = -0.5$ MAD at $T = 25,000M$.

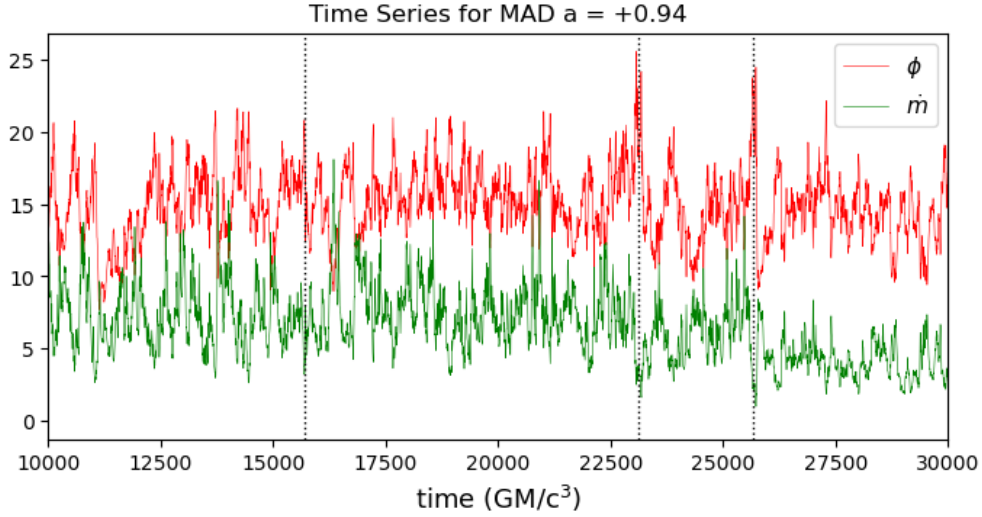


Figure 6.9: Temporal evolution of the MAD $a = +0.94$ simulation with horizon threading flux ϕ (red) and mass accretion rate \dot{m} (green) for $T = 10,000M - 30,000M$.

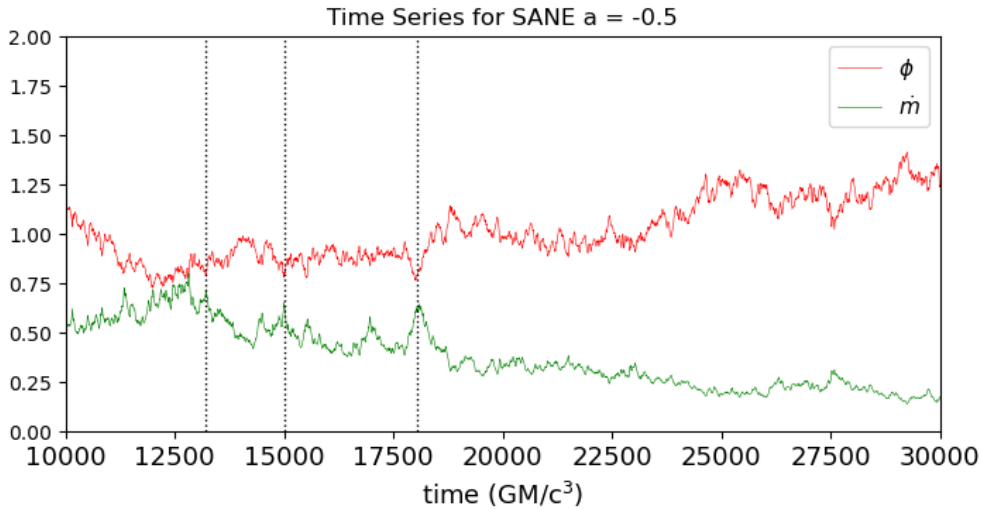


Figure 6.10: Temporal evolution of the SANE $a = -0.5$ simulation with horizon threading flux ϕ (red) and mass accretion rate \dot{m} (green) for $T = 10,000M - 30,000M$.

Similar morphologies can be seen throughout the evolution of the MAD $a = +0.94$ fiducial simulation. Although more active in Figure 6.9, MADs still produce magnetic flux eruption events through the outward push of gas from the accretion disk [23]. This is seen in Figure 6.9 for large flux eruption spikes towards the end of the temporal evolution of the simulation.

As expected for the SANE, there is no visible flux eruption throughout the evolution of the

simulation, consistent with their negligible magnetic field flux. Figure 6.10 depicts an inverse of MAD behavior with an increase in mass accretion rate onto the disk accompanied by a decrease in horizon-threading flux at certain fiducial times.

6.4 Modeling with Positrons

We observe how the inclusion of positrons changes the morphology of our models. Figures 6.11 and 6.12 depict how the R - β model changes for a SANE. We see changes in the rotation and diminishing length of the EVPAs and a large increase in circular polarization when positrons are added. These images are produced with $R_{low} = 1$ and $R_{high} = 20$ at $T = 20,000M$ for a spin of $a = -0.5$.

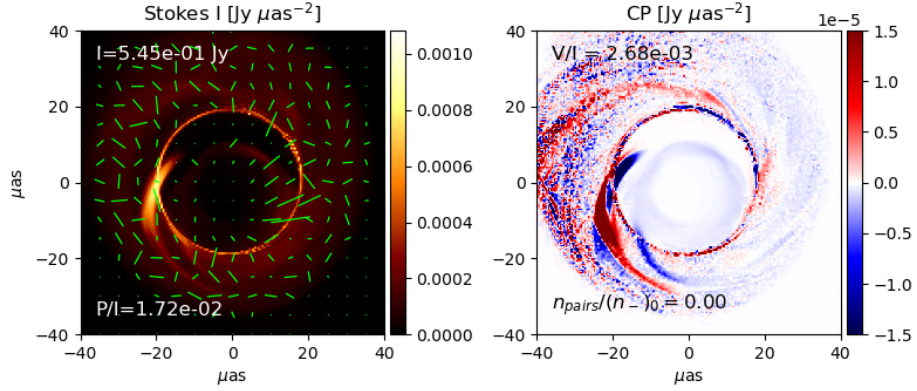


Figure 6.11: $R - \beta$ SANE model with jet inclusion from IPOLE with zero electron-positron pair fraction for $a = -0.5$ and $T = 20,000M$ for the 230 GHz emission.

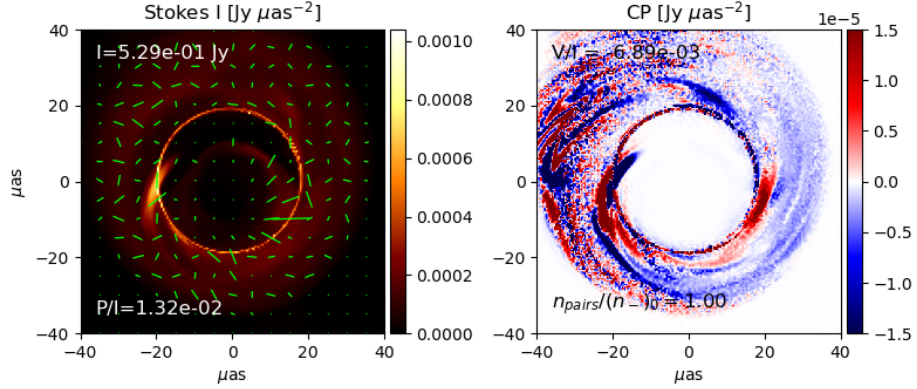


Figure 6.12: $R - \beta$ SANE model with jet inclusion from IPOLE with equal electron-positron pair fraction for $a = -0.5$ and $T = 20,000M$ for the 230 GHz emission.

Figures 6.13 and 6.14 depict how the $R-\beta$ model changes for a MAD. These images are produced with $R_{low} = 1$ and $R_{high} = 20$ at $T = 20,000M$ for a spin of $a = -0.5$. Although there is no large changes in EVPAs, we notice an increase in circular polarization as positrons are included.

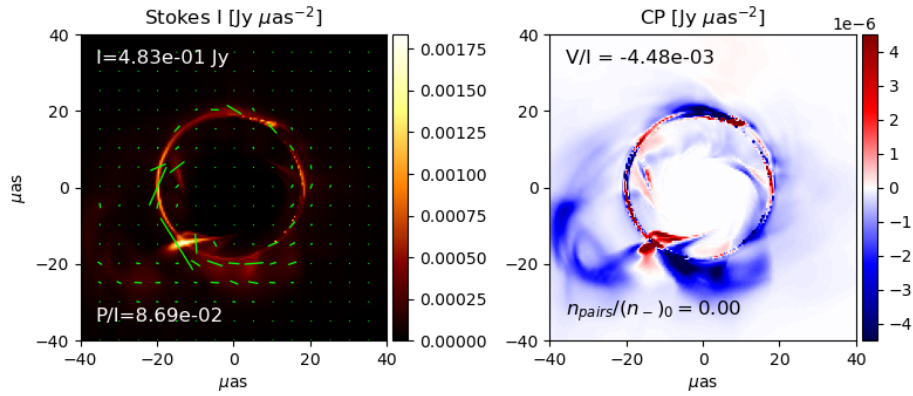


Figure 6.13: $R - \beta$ MAD model with jet inclusion from IPOLE with zero electron-positron pair fraction for $a = -0.5$ and $T = 20,000M$ for the 230 GHz emission.

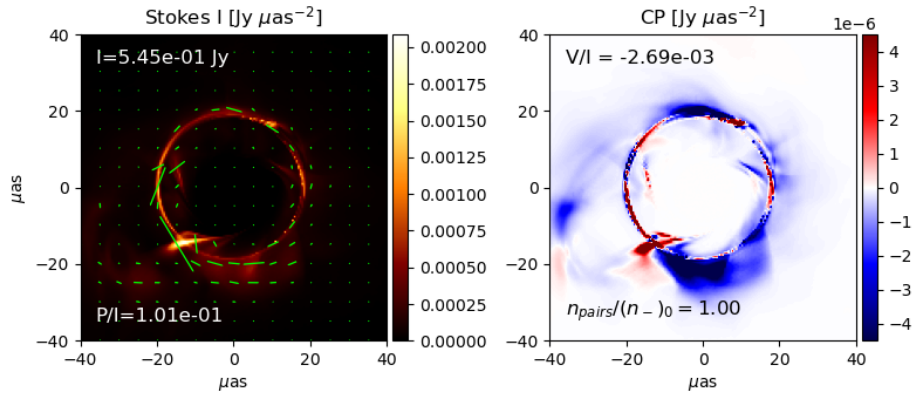


Figure 6.14: $R - \beta$ MAD model with jet inclusion from IPOLE with equal electron-positron pair fraction for $a = -0.5$ and $T = 20,000M$ for the 230 GHz emission.

We see distinct changes for the $R - \beta$ not only when positrons are included in the models, but also stark differences between MADs and SANEs. This dichotomy depicts the distinguishable differences for both accretion flow states.

CHAPTER 7: CONCLUSIONS AND FUTURE DIRECTIONS

We presented an expanding investigation into emission modeling through turbulent heating processes of EHT’s well-studied source M87. Despite large advances in the last few decades over theoretically and computationally modeling emission processes, there is still room for improvement in matching simulated data to observational constraints. We aimed to bridge that gap by expanding previously unexplored parameter spaces to see where they fall within observational constraints to showcase the viability of different turbulent heating models.

In this thesis, we outlined a pipeline for creating a library of polarimetric images and corresponding spectra for the full parameter set investigated for both the R- β model and the Critical- β model. By expanding the SANE parameter space to include the spin $a = +0.94$, we are able to probe the polarization effects beyond what was achieved in [17]. We note the shortened timesteps computed in this work in comparison to [17] and will explore how polarization changes for this expanded search when analyzed over the entire duration of the available temporal evolution as a future direction (i.e. $T = 10,000 - 30,000 GM_{M87}/c^3$). In addition, models where equal electron-positron pairs were introduced pass circular and linear polarization constraints nearly as often as standard ion-electron dominated plasma as seen in Section 6.1.1.

Our primary findings are as follows:

- Expanded parameter set of Critical- β values tested for M87 for the first time
- Critical- β passes more polarization constraints than R- β
- MADs and SANEs differ in both their circular and linear polarization values. MADs pass more of the EHT constraint for both circular and linear polarization
- No fiducial SANE models pass the β_2 constraint while few MADs pass
- We found MADs and SANEs differ wildly in their temporal evolution for the fiducial models including the large flux eruption events for both $a = -0.5$ and $+0.94$ in MADs while SANEs

appear to have the opposite effect. This depicts the difference in magnetic fields for both accretion flows.

- When the plasma is electron-positron pair dominated over electron-ion dominated, the model has an overall higher polarization value and slightly varying EVPAs.
- Synchrotron emission in our spectra is consistent with observations at 230 GHz
- Consistent trend of lower bremsstrahlung contribution from Critical- β model when compared against SEDs of R- β within the expanded parameter space

The verification of lower bremsstrahlung trend in the Critical- β Model has gone beyond what EHT has currently explored and may serve as a push to further investigate Critical- β in the same light going forward. This is another step in verifying the Critical- β model to become a strong candidate to the opposing, widely used R- β model.

Going forward, modifications can be into both GRMONTY and IPOLE to accurately capture the phenomenology we wish to investigate. There is currently no inclusion into GRMONTY to resolve the relativistic jet or include positrons. By introducing a similar σ_{cut} as in IPOLE, we could accurately resolve a jet region as currently done in IPOLE and compare our simulated images with new SED for our models that include a jet. Similarly, by including electron-positron pair plasma, we could observe how the SED differs from a standard ion-electron dominated plasma. While IPOLE currently harbors both of these modifications, an additional change we wish to implement into IPOLE is to modify positrons locally. By individually tracking the positrons, we can better account for their movement and dissipation throughout the turbulent plasma in the accretion disk.

We plan to extend this investigation into emission modeling to Sgr A* following [16]. Although already tested for the parameters listed in Table 5.3, by extending the analysis to our SED framework, we can better understand the turbulent heating mechanism in the same light as we have done here with M87.

The observing JAB phenomenology can be applied to other well-studied EHT sources such as 3C 279, a variable and interesting source on EHT's radar. This similar deep dive into observing the

Models Tested							
Model	Mode	$i[^\circ]$	a_*	R_{high}	R_{low}	f	β_c
Critical- β	MAD	163°	-0.5	-	-	0.5	1.0
Critical- β	MAD	163°	+0.94	-	-	0.5	1.0
Critical- β	MAD	163°	-0.5	-	-	0.5	0.1
Critical- β	MAD	163°	+0.94	-	-	0.5	0.1
Critical- β	SANE	163°	-0.5	-	-	0.5	1.0
Critical- β	SANE	163°	+0.94	-	-	0.5	1.0
R- β	MAD	163°	-0.5	20	1	-	1.0
R- β	MAD	163°	+0.94	20	1	-	1.0
R- β	SANE	163°	-0.5	20	1	-	1.0
R- β	SANE	163°	+0.94	20	1	-	1.0
Future Models to be Tested							
Model	Mode	$i[^\circ]$	a_*	R_{high}	R_{low}	f	β_c
Critical- β	SANE	163°	-0.5	-	-	0.5	0.1
Critical- β	SANE	163°	+0.94	-	-	0.5	0.1
Critical- β	MAD	163°	-0.5	-	-	0.5	0.01
Critical- β	MAD	163°	+0.94	-	-	0.5	0.01
R- β	MAD	163°	-0.5	40	1	-	1.0
R- β	MAD	163°	+0.94	40	1	-	1.0
R- β	SANE	163°	-0.5	40	1	-	1.0
R- β	SANE	163°	+0.94	40	1	-	1.0

Table 7.1: Values that have been tested in this thesis alongside values that will be tested for future investigations. Every row will be tested for all three fiducial timesteps of $T = 20, 000M$, $25, 000M$, and $30, 000M$ as well as computed polarimetric images through IPOLE for both ion-electron plasma and electron-positron plasma.

emission and morphology throughout the temporal simulation can be produced in the same light for a different source to see how well 3C 279 fits within EHT’s observed constraints using our framework.

Overall, we will continue to expand the parameter space beyond what was investigated here to study more R_{high} values in the R- β model as well as compare those additional R_{high} values with overlapping parameters in the Critical- β model as laid out in Table 7.1. This initiative will serve as an extension of the turbulent emission analysis.

APPENDIX A: FULL POLARIZATION TABLES

Listed below are the circular and linear polarization tables for the individual three timesteps in our simulations ($T = 20,000M - 30,000M$).

	SANE ($a = -0.5$)				MAD ($a = -0.5$)			
	$R-\beta$	$R-\beta$	Crit $-\beta$	Crit $-\beta$	$R-\beta$	$R-\beta$	Crit $-\beta$	Crit $-\beta$
		w./ Jet		w./ Jet		w./ Jet		w./ Jet
$ m _{net}(f_{pos,min})$	$1.08 \cdot 10^{-2}$	$1.71 \cdot 10^{-2}$	$2.24 \cdot 10^{-3}$	$6.80 \cdot 10^{-3}$	$8.69 \cdot 10^{-2}$	$6.21 \cdot 10^{-2}$	$6.49 \cdot 10^{-2}$	$4.63 \cdot 10^{-2}$
$ m _{net}(f_{pos,max})$	$5.37 \cdot 10^{-3}$	$1.32 \cdot 10^{-2}$	$1.86 \cdot 10^{-3}$	$1.21 \cdot 10^{-2}$	$1.01 \cdot 10^{-1}$	$7.06 \cdot 10^{-2}$	$9.76 \cdot 10^{-2}$	$7.00 \cdot 10^{-2}$
$\langle m \rangle (f_{pos,min})$	$7.72 \cdot 10^{-1}$	$9.01 \cdot 10^{-2}$	$7.83 \cdot 10^{-2}$	$9.41 \cdot 10^{-2}$	$3.71 \cdot 10^{-1}$	$3.24 \cdot 10^{-1}$	$3.01 \cdot 10^{-1}$	$2.79 \cdot 10^{-1}$
$\langle m \rangle (f_{pos,max})$	$8.32 \cdot 10^{-2}$	$1.00 \cdot 10^{-1}$	$8.27 \cdot 10^{-2}$	$1.04 \cdot 10^{-1}$	$4.74 \cdot 10^{-1}$	$4.15 \cdot 10^{-1}$	$4.12 \cdot 10^{-1}$	$3.91 \cdot 10^{-1}$
	SANE ($a = +0.94$)				MAD ($a = +0.94$)			
	$R-\beta$	$R-\beta$	Crit $-\beta$	Crit $-\beta$	$R-\beta$	$R-\beta$	Crit $-\beta$	Crit $-\beta$
		w./ Jet		w./ Jet		w./ Jet		w./ Jet
$ m _{net}(f_{pos,min})$	$2.69 \cdot 10^{-2}$	$1.86 \cdot 10^{-2}$	$1.95 \cdot 10^{-2}$	$1.74 \cdot 10^{-2}$	$6.58 \cdot 10^{-2}$	$5.77 \cdot 10^{-2}$	$5.54 \cdot 10^{-2}$	$15.41 \cdot 10^{-2}$
$ m _{net}(f_{pos,max})$	$3.41 \cdot 10^{-2}$	$2.25 \cdot 10^{-2}$	$2.62 \cdot 10^{-2}$	$1.64 \cdot 10^{-2}$	$6.02 \cdot 10^{-2}$	$5.01 \cdot 10^{-2}$	$7.19 \cdot 10^{-2}$	$6.21 \cdot 10^{-2}$
$\langle m \rangle (f_{pos,min})$	$3.40 \cdot 10^{-2}$	$2.19 \cdot 10^{-1}$	$2.18 \cdot 10^{-1}$	$2.24 \cdot 10^{-1}$	$5.93 \cdot 10^{-1}$	$5.36 \cdot 10^{-1}$	$5.65 \cdot 10^{-1}$	$5.22 \cdot 10^{-1}$
$\langle m \rangle (f_{pos,max})$	$2.13 \cdot 10^{-1}$	$2.30 \cdot 10^{-1}$	$2.22 \cdot 10^{-1}$	$2.31 \cdot 10^{-1}$	$5.91 \cdot 10^{-1}$	$5.37 \cdot 10^{-1}$	$5.92 \cdot 10^{-1}$	$5.43 \cdot 10^{-1}$

Table A.1: Linear polarization for $|m_{net}|$ and $\langle |m| \rangle$ for $T = 20,000M$. From [8], observational constraints were found to be $0.01 \leq |m_{net}| \leq 0.037$ and $0.057 \ll \langle |m| \rangle \ll 0.107$. The bold values refer to values that satisfy the linear polarization constraints.

	SANE ($a = -0.5$)				MAD ($a = -0.5$)			
	$R-\beta$	$R-\beta$	Crit $-\beta$	Crit $-\beta$	$R-\beta$	$R-\beta$	Crit $-\beta$	Crit $-\beta$
		w./ Jet		w./ Jet		w./ Jet		w./ Jet
$ V _{net}(f_{pos,min})$	$1.23 \cdot 10^{-2}$	$2.68 \cdot 10^{-3}$	$3.64 \cdot 10^{-2}$	$1.72 \cdot 10^{-2}$	$-4.49 \cdot 10^{-3}$	$-3.33 \cdot 10^{-3}$	$-3.58 \cdot 10^{-3}$	$-3.02 \cdot 10^{-3}$
$ V _{net}(f_{pos,max})$	$1.41 \cdot 10^{-2}$	$-6.89 \cdot 10^{-3}$	$5.52 \cdot 10^{-2}$	$1.04 \cdot 10^{-2}$	$-2.69 \cdot 10^{-3}$	$-1.36 \cdot 10^{-3}$	$-3.19 \cdot 10^{-3}$	$1.54 \cdot 10^{-3}$
$\langle V \rangle (f_{pos,min})$	$1.47 \cdot 10^{-2}$	$8.65 \cdot 10^{-3}$	$4.43 \cdot 10^{-2}$	$3.07 \cdot 10^{-2}$	$3.60 \cdot 10^{-3}$	$2.76 \cdot 10^{-3}$	$3.26 \cdot 10^{-3}$	$2.56 \cdot 10^{-3}$
$\langle V \rangle (f_{pos,max})$	$2.11 \cdot 10^{-2}$	$1.70 \cdot 10^{-2}$	$7.25 \cdot 10^{-2}$	$3.96 \cdot 10^{-2}$	$1.28 \cdot 10^{-3}$	$7.05 \cdot 10^{-4}$	$1.45 \cdot 10^{-3}$	$7.64 \cdot 10^{-4}$
	SANE ($a = +0.94$)				MAD ($a = +0.94$)			
	$R-\beta$	$R-\beta$	Crit $-\beta$	Crit $-\beta$	$R-\beta$	$R-\beta$	Crit $-\beta$	Crit $-\beta$
		w./ Jet		w./ Jet		w./ Jet		w./ Jet
$ V _{net}(f_{pos,min})$	$-1.54 \cdot 10^{-2}$	$-1.06 \cdot 10^{-2}$	$-2.19 \cdot 10^{-2}$	$-2.37 \cdot 10^{-2}$	$-1.69 \cdot 10^{-3}$	$-1.71 \cdot 10^{-3}$	$-2.16 \cdot 10^{-3}$	$-1.90 \cdot 10^{-3}$
$ V _{net}(f_{pos,max})$	$-4.63 \cdot 10^{-2}$	$-4.41 \cdot 10^{-3}$	$-3.03 \cdot 10^{-2}$	$-3.84 \cdot 10^{-2}$	$-1.30 \cdot 10^{-4}$	$-3.63 \cdot 10^{-4}$	$-4.54 \cdot 10^{-4}$	$-4.60 \cdot 10^{-4}$
$\langle V \rangle (f_{pos,min})$	$9.06 \cdot 10^{-3}$	$1.40 \cdot 10^{-2}$	$2.30 \cdot 10^{-2}$	$3.62 \cdot 10^{-2}$	$2.91 \cdot 10^{-3}$	$2.08 \cdot 10^{-3}$	$2.90 \cdot 10^{-3}$	$2.14 \cdot 10^{-3}$
$\langle V \rangle (f_{pos,max})$	$1.80 \cdot 10^{-2}$	$3.62 \cdot 10^{-2}$	$3.43 \cdot 10^{-2}$	$6.85 \cdot 10^{-2}$	$6.85 \cdot 10^{-4}$	$3.65 \cdot 10^{-4}$	$6.51 \cdot 10^{-4}$	$3.94 \cdot 10^{-4}$

Table A.2: Circular polarization for $|V|_{net}$ and $\langle |V| \rangle$ for $T = 20,000M$. The bold models satisfy the EHT limit of $-8.0 \cdot 10^{-3} V_{net} < 8.0 \cdot 10^{-3}$ and $0 \ll \langle |V| \rangle \ll 3.7 \cdot 10^{-2}$.

	$R-\beta$	SANE $R-\beta$ w./ Jet	($a = -0.5$) Crit $-\beta$	Crit $-\beta$ w./ Jet	$R-\beta$	MAD $R-\beta$ w./ Jet	($a = -0.5$) Crit $-\beta$	Crit $-\beta$ w./ Jet
$ m _{net}(f_{pos,min})$	$3.92 \cdot 10^{-3}$	$4.77 \cdot 10^{-3}$	$8.53 \cdot 10^{-3}$	$5.69 \cdot 10^{-3}$	$5.51 \cdot 10^{-2}$	$4.07 \cdot 10^{-2}$	$6.93 \cdot 10^{-2}$	$4.86 \cdot 10^{-2}$
$ m _{net}(f_{pos,max})$	$1.62 \cdot 10^{-3}$	$6.29 \cdot 10^{-3}$	$2.73 \cdot 10^{-3}$	$6.14 \cdot 10^{-3}$	$3.67 \cdot 10^{-2}$	$3.10 \cdot 10^{-2}$	$5.21 \cdot 10^{-2}$	$3.53 \cdot 10^{-2}$
$\langle m \rangle (f_{pos,min})$	$1.29 \cdot 10^{-1}$	$1.42 \cdot 10^{-2}$	$1.35 \cdot 10^{-1}$	$1.46 \cdot 10^{-1}$	$3.49 \cdot 10^{-1}$	$3.30 \cdot 10^{-1}$	$2.71 \cdot 10^{-1}$	$2.53 \cdot 10^{-1}$
$\langle m \rangle (f_{pos,max})$	$1.31 \cdot 10^{-1}$	$1.49 \cdot 10^{-1}$	$1.39 \cdot 10^{-1}$	$1.50 \cdot 10^{-1}$	$4.20 \cdot 10^{-1}$	$3.60 \cdot 10^{-1}$	$3.83 \cdot 10^{-1}$	$3.46 \cdot 10^{-1}$
	$R-\beta$	SANE $R-\beta$ w./ Jet	($a = +0.94$) Crit $-\beta$	Crit $-\beta$ w./ Jet	$R-\beta$	MAD $R-\beta$ w./ Jet	($a = +0.94$) Crit $-\beta$	Crit $-\beta$ w./ Jet
$ m _{net}(f_{pos,min})$	$1.05 \cdot 10^{-2}$	$1.41 \cdot 10^{-2}$	$1.47 \cdot 10^{-2}$	$1.82 \cdot 10^{-3}$	$4.91 \cdot 10^{-2}$	$4.56 \cdot 10^{-2}$	$3.07 \cdot 10^{-1}$	$3.67 \cdot 10^{-1}$
$ m _{net}(f_{pos,max})$	$2.80 \cdot 10^{-2}$	$1.06 \cdot 10^{-2}$	$9.02 \cdot 10^{-3}$	$7.39 \cdot 10^{-3}$	$5.17 \cdot 10^{-2}$	$5.06 \cdot 10^{-2}$	$4.38 \cdot 10^{-2}$	$4.82 \cdot 10^{-2}$
$\langle m \rangle (f_{pos,min})$	$2.35 \cdot 10^{-1}$	$2.58 \cdot 10^{-1}$	$1.94 \cdot 10^{-1}$	$1.98 \cdot 10^{-1}$	$5.76 \cdot 10^{-1}$	$5.18 \cdot 10^{-1}$	$4.98 \cdot 10^{-1}$	$4.88 \cdot 10^{-1}$
$\langle m \rangle (f_{pos,max})$	$2.39 \cdot 10^{-1}$	$2.65 \cdot 10^{-1}$	$2.00 \cdot 10^{-1}$	$2.14 \cdot 10^{-1}$	$5.86 \cdot 10^{-1}$	$5.52 \cdot 10^{-1}$	$5.76 \cdot 10^{-1}$	$5.26 \cdot 10^{-1}$

Table A.3: Linear polarization for $|m_{net}|$ and $\langle |m| \rangle$ for $T = 25, 000M$. From [8], observational constraints were found to be $0.01 \leq |m_{net}| \leq 0.037$ and $0.057 \ll \langle |m| \rangle < 0.107$. The bold values refer to values that satisfy the linear polarization constraints.

	$R-\beta$	SANE $R-\beta$ w./ Jet	($a = -0.5$) Crit $-\beta$	Crit $-\beta$ w./ Jet	$R-\beta$	MAD $R-\beta$ w./ Jet	($a = -0.5$) Crit $-\beta$	Crit $-\beta$ w./ Jet
$ V _{net}(f_{pos,min})$	$-5.60 \cdot 10^{-3}$	$-1.68 \cdot 10^{-3}$	$7.78 \cdot 10^{-3}$	$-2.86 \cdot 10^{-3}$	$-4.50 \cdot 10^{-3}$	$-3.53 \cdot 10^{-3}$	$-4.24 \cdot 10^{-3}$	$-3.58 \cdot 10^{-3}$
$ V _{net}(f_{pos,max})$	$-2.81 \cdot 10^{-3}$	$2.59 \cdot 10^{-3}$	$3.15 \cdot 10^{-3}$	$1.40 \cdot 10^{-3}$	$-1.39 \cdot 10^{-3}$	$-8.99 \cdot 10^{-4}$	$-1.19 \cdot 10^{-3}$	$-8.45 \cdot 10^{-4}$
$\langle V \rangle (f_{pos,min})$	$6.75 \cdot 10^{-3}$	$4.69 \cdot 10^{-3}$	$8.94 \cdot 10^{-3}$	$6.57 \cdot 10^{-3}$	$3.98 \cdot 10^{-3}$	$2.96 \cdot 10^{-3}$	$3.82 \cdot 10^{-3}$	$3.03 \cdot 10^{-3}$
$\langle V \rangle (f_{pos,max})$	$1.28 \cdot 10^{-2}$	$6.41 \cdot 10^{-3}$	$2.32 \cdot 10^{-2}$	$1.06 \cdot 10^{-2}$	$9.04 \cdot 10^{-4}$	$5.75 \cdot 10^{-4}$	$8.57 \cdot 10^{-4}$	$5.66 \cdot 10^{-4}$
	$R-\beta$	SANE $R-\beta$ w./ Jet	($a = +0.94$) Crit $-\beta$	Crit $-\beta$ w./ Jet	$R-\beta$	MAD $R-\beta$ w./ Jet	($a = +0.94$) Crit $-\beta$	Crit $-\beta$ w./ Jet
$ V _{net}(f_{pos,min})$	$2.63 \cdot 10^{-2}$	$4.24 \cdot 10^{-2}$	$1.99 \cdot 10^{-2}$	$2.96 \cdot 10^{-2}$	$-3.63 \cdot 10^{-3}$	$-2.33 \cdot 10^{-3}$	$-3.31 \cdot 10^{-3}$	$-2.41 \cdot 10^{-3}$
$ V _{net}(f_{pos,max})$	$5.78 \cdot 10^{-2}$	$7.61 \cdot 10^{-2}$	$1.35 \cdot 10^{-2}$	$2.32 \cdot 10^{-2}$	$-1.13 \cdot 10^{-3}$	$-7.37 \cdot 10^{-4}$	$-1.80 \cdot 10^{-3}$	$-7.29 \cdot 10^{-4}$
$\langle V \rangle (f_{pos,min})$	$6.65 \cdot 10^{-3}$	$1.20 \cdot 10^{-2}$	$8.97 \cdot 10^{-3}$	$1.62 \cdot 10^{-2}$	$3.17 \cdot 10^{-3}$	$2.17 \cdot 10^{-3}$	$3.13 \cdot 10^{-3}$	$2.19 \cdot 10^{-3}$
$\langle V \rangle (f_{pos,max})$	$1.52 \cdot 10^{-2}$	$2.62 \cdot 10^{-2}$	$6.48 \cdot 10^{-3}$	$1.41 \cdot 10^{-2}$	$7.62 \cdot 10^{-4}$	$5.02 \cdot 10^{-4}$	$1.05 \cdot 10^{-3}$	$4.86 \cdot 10^{-4}$

Table A.4: Circular polarization for $|V|_{net}$ and $\langle |V| \rangle$ for $T = 25, 000M$. The bold models satisfy the EHT limit of $-8.0 \cdot 10^{-3} V_{net} < 8.0 \cdot 10^{-3}$ and $0 \ll \langle |V| \rangle < 3.7 \cdot 10^{-2}$.

	$R-\beta$	SANE $R-\beta$ w./ Jet	($a = -0.5$) Crit $-\beta$	Crit $-\beta$ w./ Jet	$R-\beta$	MAD $R-\beta$ w./ Jet	($a = -0.5$) Crit $-\beta$	Crit $-\beta$ w./ Jet
$ m _{net}(f_{pos,min})$	$5.00 \cdot 10^{-3}$	$4.95 \cdot 10^{-3}$	$7.90 \cdot 10^{-4}$	$1.75 \cdot 10^{-4}$	$6.71 \cdot 10^{-2}$	$4.34 \cdot 10^{-2}$	$5.49 \cdot 10^{-2}$	$4.46 \cdot 10^{-2}$
$ m _{net}(f_{pos,max})$	$8.74 \cdot 10^{-3}$	$4.82 \cdot 10^{-3}$	$4.48 \cdot 10^{-3}$	$8.31 \cdot 10^{-4}$	$5.52 \cdot 10^{-2}$	$2.43 \cdot 10^{-2}$	$5.68 \cdot 10^{-2}$	$2.67 \cdot 10^{-2}$
$\langle m \rangle (f_{pos,min})$	$1.39 \cdot 10^{-1}$	$1.46 \cdot 10^{-2}$	$1.45 \cdot 10^{-1}$	$1.52 \cdot 10^{-1}$	$3.17 \cdot 10^{-1}$	$3.15 \cdot 10^{-1}$	$2.52 \cdot 10^{-1}$	$2.61 \cdot 10^{-1}$
$\langle m \rangle (f_{pos,max})$	$1.40 \cdot 10^{-1}$	$1.48 \cdot 10^{-1}$	$1.46 \cdot 10^{-1}$	$1.53 \cdot 10^{-1}$	$4.63 \cdot 10^{-1}$	$4.45 \cdot 10^{-1}$	$4.02 \cdot 10^{-1}$	$4.06 \cdot 10^{-1}$
	$R-\beta$	SANE $R-\beta$ w./ Jet	($a = +0.94$) Crit $-\beta$	Crit $-\beta$ w./ Jet	$R-\beta$	MAD $R-\beta$ w./ Jet	($a = +0.94$) Crit $-\beta$	Crit $-\beta$ w./ Jet
$ m _{net}(f_{pos,min})$	$1.69 \cdot 10^{-2}$	$6.33 \cdot 10^{-3}$	$1.64 \cdot 10^{-2}$	$1.18 \cdot 10^{-2}$	$3.21 \cdot 10^{-2}$	$2.50 \cdot 10^{-2}$	$1.19 \cdot 10^{-2}$	$6.00 \cdot 10^{-3}$
$ m _{net}(f_{pos,max})$	$2.30 \cdot 10^{-2}$	$2.34 \cdot 10^{-2}$	$6.35 \cdot 10^{-3}$	$8.76 \cdot 10^{-3}$	$4.46 \cdot 10^{-2}$	$2.80 \cdot 10^{-2}$	$1.39 \cdot 10^{-1}$	$1.35 \cdot 10^{-2}$
$\langle m \rangle (f_{pos,min})$	$2.25 \cdot 10^{-1}$	$2.65 \cdot 10^{-1}$	$2.17 \cdot 10^{-1}$	$2.53 \cdot 10^{-1}$	$5.74 \cdot 10^{-1}$	$5.22 \cdot 10^{-1}$	$5.06 \cdot 10^{-1}$	$4.77 \cdot 10^{-1}$
$\langle m \rangle (f_{pos,max})$	$2.30 \cdot 10^{-1}$	$2.75 \cdot 10^{-1}$	$2.16 \cdot 10^{-1}$	$2.63 \cdot 10^{-1}$	$5.81 \cdot 10^{-1}$	$5.32 \cdot 10^{-1}$	$5.68 \cdot 10^{-1}$	$5.27 \cdot 10^{-1}$

Table A.5: Linear polarization for $|m_{net}|$ and $\langle |m| \rangle$ for $T = 30, 000M$. From [8], observational constraints were found to be $0.01 \leq |m_{net}| \leq 0.037$ and $0.057 \ll \langle |m| \rangle < 0.107$. The bold values refer to values that satisfy the linear polarization constraints.

	$R-\beta$	SANE $R-\beta$ w./ Jet	($a = -0.5$) Crit - β	Crit - β w./ Jet	$R-\beta$	MAD $R-\beta$ w./ Jet	($a = -0.5$) Crit - β	Crit - β w./ Jet
$ V _{net}(f_{pos,min})$	$-7.11 \cdot 10^{-3}$	$-2.37 \cdot 10^{-3}$	$-2.17 \cdot 10^{-3}$	$5.48 \cdot 10^{-3}$	$-1.98 \cdot 10^{-3}$	$-1.58 \cdot 10^{-3}$	$-1.89 \cdot 10^{-3}$	$-1.40 \cdot 10^{-3}$
$ V _{net}(f_{pos,max})$	$1.04 \cdot 10^{-2}$	$6.43 \cdot 10^{-3}$	$5.85 \cdot 10^{-2}$	$2.64 \cdot 10^{-2}$	$-2.10 \cdot 10^{-3}$	$-9.43 \cdot 10^{-4}$	$-1.67 \cdot 10^{-3}$	$-1.03 \cdot 10^{-3}$
$\langle V \rangle (f_{pos,min})$	$8.39 \cdot 10^{-3}$	$4.94 \cdot 10^{-3}$	$1.27 \cdot 10^{-2}$	$7.33 \cdot 10^{-3}$	$2.67 \cdot 10^{-3}$	$2.08 \cdot 10^{-3}$	$2.69 \cdot 10^{-3}$	$2.04 \cdot 10^{-3}$
$\langle V \rangle (f_{pos,max})$	$1.18 \cdot 10^{-2}$	$4.86 \cdot 10^{-3}$	$2.63 \cdot 10^{-2}$	$1.15 \cdot 10^{-2}$	$9.32 \cdot 10^{-4}$	$5.48 \cdot 10^{-4}$	$7.51 \cdot 10^{-4}$	$5.60 \cdot 10^{-4}$
	$R-\beta$	SANE $R-\beta$ w./ Jet	($a = +0.94$) Crit - β	Crit - β w./ Jet	$R-\beta$	MAD $R-\beta$ w./ Jet	($a = +0.94$) Crit - β	Crit - β w./ Jet
$ V _{net}(f_{pos,min})$	$2.12 \cdot 10^{-2}$	$4.06 \cdot 10^{-2}$	$1.20 \cdot 10^{-3}$	$-3.91 \cdot 10^{-4}$	$-4.57 \cdot 10^{-4}$	$-8.88 \cdot 10^{-4}$	$-1.37 \cdot 10^{-3}$	$-1.33 \cdot 10^{-3}$
$ V _{net}(f_{pos,max})$	$2.93 \cdot 10^{-2}$	$4.84 \cdot 10^{-2}$	$5.71 \cdot 10^{-3}$	$6.27 \cdot 10^{-3}$	$1.76 \cdot 10^{-3}$	$4.65 \cdot 10^{-4}$	$9.03 \cdot 10^{-4}$	$2.61 \cdot 10^{-4}$
$\langle V \rangle (f_{pos,min})$	$5.86 \cdot 10^{-3}$	$1.12 \cdot 10^{-2}$	$4.02 \cdot 10^{-3}$	$7.68 \cdot 10^{-3}$	$2.04 \cdot 10^{-3}$	$1.45 \cdot 10^{-3}$	$1.80 \cdot 10^{-3}$	$1.41 \cdot 10^{-3}$
$\langle V \rangle (f_{pos,max})$	$9.99 \cdot 10^{-3}$	$1.43 \cdot 10^{-2}$	$2.60 \cdot 10^{-3}$	$5.51 \cdot 10^{-3}$	$5.50 \cdot 10^{-4}$	$3.11 \cdot 10^{-4}$	$4.63 \cdot 10^{-4}$	$2.80 \cdot 10^{-4}$

Table A.6: Circular polarization for $|V|_{net}$ and $\langle |V| \rangle$ for $T = 30,000M$ The bold models satisfy the EHT limit of $-8.0 \cdot 10^{-3}V_{net} < 8.0 \cdot 10^{-3}$ and $0 < \langle |V| \rangle < 3.7 \cdot 10^{-2}$.

APPENDIX B: GRMONTY USER GUIDE

There are two versions of GRMONTY on GitHub: `igrmonty` and `igrmonty2D`. In addition, there is a branch of GRMONTY by A. Ricarte modified to use the Critical- β model. This user guide will discuss how to compile and produce a spectrum for A. Ricarte's GRMONTY.

There is a generic tutorial for compiling and creating a simple `iharm` spectrum. There is a paper describing the analytics and theory behind the Monte Carlo code used for GRMONTY.

A general UTSA ARC user guide can be found here. ARC is a Linux-based terminal, so it is necessary to be familiar with basic Linux commands, found here.

1. Importing Simulation Data

(a) KHARMA dump samples can be found in the box repository from G. Wong as `.h5` files

- i. The filenames are labeled as follows: Ma stands for MAD, Sa stands for SANE. There are two spin states (a): `-0.5` and `+0.94`. The end number gives the timestep (M) when multiplied by 5.

(b) There are two processes when trying to transfer files on ARC:

- i. Using the SCP command to transfer into the desired directory with `scp filename.h5 abc123@arc.utsa.edu:/work/abc123/yourdirectory` within the ARC terminal
- ii. Using a second party application WinSCP to upload

2. Compiling GRMONTY

(a) Now that the files are on ARC, we are ready to download and compile GRMONTY.

- i. To log onto the terminal, it is easiest for Mac users to use the terminal and for Windows users to use MobaXterm
- ii. To properly log onto a MobaXterm session, follow these steps:

- A. Click `Session` in the far-left corner of the application, and then `SSH` in the next pop-up box
 - B. Enter the following to access ARC in the `Basic SSH settings`: Remote host: `arc.utsa.edu` Specify username: `abc123` Port: `22`
 - C. After logging on, you will be prompted to enter your UTSA password and use two-factor authorization to confirm your identity
 - D. After hitting `OK`, you should see a screen similar to this. You are now logged into the ARC cluster
- iii. Create a directory for `GRMONTY` using the command `mkdir GRMONTY` or any name you prefer to use for the directory
 - iv. Move into the new directory using `cd GRMONTY`. To download the version with multiple models, use the clone command `git clone` followed by the url to the repository
 - v. We now need to load the proper modules to compile. You can always check what modules are available on arc by running `module spider`. `GRMONTY` requires `gsl` and `hdf5`. Load these by running: `module load gsl` and `module load hdf5`
 - vi. In addition to the modules, you will need to access the makefile and remove the `-static` flag in the `CFLAGS` line in order for `GRMONTY` to properly compile on ARC. Press `I` on the keyboard to modify the file and `esc` key when finished. Save and exit the file using `:wq`. This flag does not allow the needed shared libraries to be used that were previously loaded.
 - vii. At the top of the makefile, the `MODEL` should be set to `iharm`. It should be the default. We are running `GRMONTY` in the `HARM` scheme.
 - viii. `GRMONTY` can now be compiled using the command `make`
 - ix. To confirm it properly compiled, use the `ls` command and make sure `grmonty` is now green lettered instead of blue.

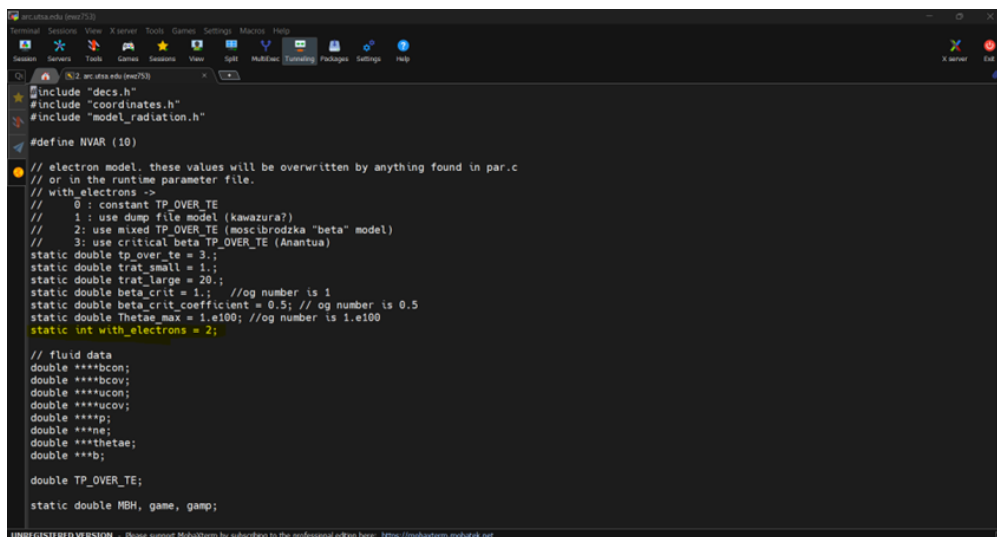
3. Choosing the Turbulent Heating Model

(a) Once compiled, you will choose which turbulent heating model you prefer to run.

While the original versions of GRMONTY are only programmed for the $R-\beta$ model, Ricarte's version has $Critical-\beta$ implemented. Here is how to modify which model you want to use

i. Move into the directory `/work/abc123/GRMONTY/model/iharm`

ii. Use the command `vi model.c` to open the file. You should see this screen:



```
incubator (ms753)
Terminal Sessions View X-server Tools Games Settings Macros Help
~/work/abc123/GRMONTY/model/iharm
#include "dcs.h"
#include "coordinates.h"
#include "model_radiation.h"

#define NVAR (10)

// electron model, these values will be overwritten by anything found in par.c
// or in the runtime parameter file.
// with_electrons ->
// 0 : constant TP_OVER_TE
// 1 : use dump file model (kawazura?)
// 2 : use mixed TP_OVER_TE (moscibrodzka "beta" model)
// 3 : use critical beta TP_OVER_TE (Anantua)
static double tp_over_te = 3.;
static double trat_small = 1.;
static double trat_large = 20.;
static double beta_crit = 1.; //og number is 1
static double beta_crit_coefficient = 0.5; // og number is 0.5
static double Thetae_max = 1.e100; //og number is 1.e100
static int with_electrons = 2;

// fluid data
double ****bcon;
double ****bcov;
double ****ucon;
double ****ucov;
double ****p;
double ****ne;
double ****thetae;
double ****b;

double TP_OVER_TE;

static double MBH, game, gamp;
```

iii. Highlighted in yellow above is the parameter to change to modify which turbulent heating model you prefer to use. Set `static int with_electrons` to 2 for $R-\beta$ model or 3 for $Critical-\beta$ model. If the modification is being overwritten when running, add `with_electrons` to the `template.par` file instead.

4. Running the Simulation

(a) After picking which model we want to run, we can now modify the parameter file. You should find the `template.par` file under `/work/abc123/GRMONTY`. Open this file using `vi template.par`

(b) This is a list of parameters you will find and edit to properly run your simulation.

Parameters in template.par file	Definitions
Fit_bias	= 1 to enable bias tuning, = 0 to disable
Fit_bias_ns	Ns used for bias tuning (smaller = fast & less accurate)
Bias	>1 for thin, <1 for thick
Ns	Number of superphotons in the spectrum
MBH	Central black hole mass
M_unit	Mass unit for the plasma in accretion flow
TP_OVER_TE	Proton-electron temperature ratio
Dump	Insert path to grmhd snapshot/dump sample
spectrum	Insert path to output spectra data to

(c) Tips for modifying your parameter file:

- i. Start with a higher number of superphotons (<500,000) to reduce noise
- ii. If there are multiple errors, decrease the bias
- iii. If the ratio is zero while running, increase the bias
- iv. Bias tuning works best when the seed value is a smaller value
- v. If preferred, comment out TP_OVER_TE and use `trat_small` and `trat_large`.
This allows you to input a specific R_{high} and R_{low} value instead of a set temperature ratio.

(d) After modifications are done, GRMONTY is ran using the command `./grmonty -par template.par`. After the run finishes, the outputted file will be in the specific directory on the spectrum line in the `template.par` file.

5. Generating a Spectrum

- (a) After the run is finished, we can generate a spectrum using the `plspec.py` file. First we need to open a virtual machine on ARC which is needed to run python.
- (b) To use a virtual machine on ARC, you need to be in an interactive session first.
 - i. To start an interactive session on a non-GPU compute node, use the command
`srun -p compute1 -n 1 -t 01:30:00 -pty bash`

- ii. To start an interactive session on a GPU node, use the command `srun -p gpubv100 -n 1 -t 01:30:00 -pty bash`
- (c) To start the virtual environment, you will need two commands:
- i. First run `module load anaconda3`
 - ii. Then `conda activate myvm` and you should see a `(myvm)` line in the terminal. The python environment is now activated.
- (d) To generate a spectrum, run the command `python3 plspect.py path/to/outputted/spectrum.h5`. A `.png` file will be produced in the same directory where the outputted `.h5` files are from the simulation.
- i. Note that you cannot see your outputted image on ARC. You will need to download it to your local device either with the SCP command or through the WinSCP app.
 - ii. Your spectrum should look similar to Figure 4.3.

BIBLIOGRAPHY

- [1] AA et al., Markus Ackermann, Marco Ajello, WB Atwood, Magnus Axelsson, Luca Baldini, Jean Ballet, Guido Barbiellini, Denis Bastieri, K Bechtol, et al. Fermi large area telescope gamma-ray detection of the radio galaxy m87. *The Astrophysical Journal*, 707(1):55, 2009.
- [2] Felix Aharonian, AG Akhperjanian, AR Bazer-Bachi, M Beilicke, Wytan Benbow, David Berge, K Bernlohr, C Boisson, Oliver Bolz, V Borrel, et al. Fast variability of tera electron volt γ rays from the radio galaxy m87. *Science*, 314(5804):1424–1427, 2006.
- [3] Kazunori Akiyama, Antxon Alberdi, Walter Alef, Juan Carlos Algaba, Richard Anantua, Keiichi Asada, Rebecca Azulay, Uwe Bach, Anne-Kathrin Baczko, David Ball, et al. First sagittarius a* event horizon telescope results. i. the shadow of the supermassive black hole in the center of the milky way. *The Astrophysical Journal Letters*, 930(2):L12, 2022.
- [4] Kazunori Akiyama, Antxon Alberdi, Walter Alef, Juan Carlos Algaba, Richard Anantua, Keiichi Asada, Rebecca Azulay, Uwe Bach, Anne-Kathrin Baczko, David Ball, et al. First sagittarius a* event horizon telescope results. v. testing astrophysical models of the galactic center black hole. *The Astrophysical Journal Letters*, 930(2):L16, 2022.
- [5] Kazunori Akiyama, Antxon Alberdi, Walter Alef, Juan Carlos Algaba, Richard Anantua, Keiichi Asada, Rebecca Azulay, Uwe Bach, Anne-Kathrin Baczko, David Ball, et al. First m87 event horizon telescope results. ix. detection of near-horizon circular polarization. *The Astrophysical Journal Letters*, 957(2):L20, 2023.
- [6] Kazunori Akiyama, Antxon Alberdi, Walter Alef, Keiichi Asada, Rebecca Azulay, Anne-Kathrin Baczko, David Ball, Mislav Baloković, John Barrett, Dan Bintley, et al. First m87 event horizon telescope results. iv. imaging the central supermassive black hole. *The Astrophysical Journal Letters*, 875(1):L4, 2019.

- [7] Kazunori Akiyama, Antxon Alberdi, Walter Alef, Keiichi Asada, Rebecca Azulay, Anne-Kathrin Baczko, David Ball, Mislav Baloković, John Barrett, Dan Bintley, et al. First m87 event horizon telescope results. v. physical origin of the asymmetric ring. *The Astrophysical Journal Letters*, 875(1):L5, 2019.
- [8] Kazunori Akiyama, Juan Carlos Algaba, Antxon Alberdi, Walter Alef, Richard Anantua, Keiichi Asada, Rebecca Azulay, Anne-Kathrin Baczko, David Ball, Mislav Baloković, et al. First m87 event horizon telescope results. vii. polarization of the ring. *The Astrophysical Journal Letters*, 910(1):L12, 2021.
- [9] Hannes Alfvén. Existence of electromagnetic-hydrodynamic waves. *Nature*, 150(3805):405–406, 1942.
- [10] JC Algaba, M Baloković, S Chandra, W-Y Cheong, Y-Z Cui, F dâAmmando, AD Falcone, NM Ford, M Giroletti, C Goddi, et al. Broadband multi-wavelength properties of m87 during the 2018 eht campaign including a very high energy flaring episode. *Astronomy & Astrophysics*, 692:A140, 2024.
- [11] Juan-Carlos Algaba, Jady Ancyarski, Keiichi Asada, Mislav Baloković, S Chandra, Y-Z Cui, AD Falcone, MARCELLO Giroletti, C Goddi, K Hada, et al. Broadband multi-wavelength properties of m87 during the 2017 event horizon telescope campaign. *The Astrophysical Journal Letters*, 911(1):L11, 2021.
- [12] Juan-Carlos Algaba, Jady Ancyarski, Keiichi Asada, Mislav Baloković, S Chandra, Y-Z Cui, AD Falcone, MARCELLO Giroletti, Ciriaco Goddi, K Hada, et al. Broadband multi-wavelength properties of m87 during the 2017 event horizon telescope campaign. *The Astrophysical Journal Letters*, 911(1):L11, 2021.
- [13] Richard Anantua, Joaquín Dúran, Nathan Ngata, Lani Oramas, Jan Röder, Razieh Emami, Angelo Ricarte, Brandon Curd, Avery E Broderick, Jeremy Wayland, et al. Emission modeling in the eht–ngeht age. *Galaxies*, 11(1):4, 2022.

- [14] Richard Anantua, Joaquín Dúran, Nathan Ngata, Lani Oramas, Jan Röder, Razieh Emami, Angelo Ricarte, Brandon Curd, Avery E. Broderick, Jeremy Wayland, George N. Wong, Sean Ressler, Nitya Nigam, and Emmanuel Durodola. Emission Modeling in the EHT–ngEHT Age. *Galaxies*, 11(1):4, jan 2023.
- [15] Richard Anantua, Razieh Emami, Abraham Loeb, and Andrew Chael. Determining the composition of relativistic jets from polarization maps. *The Astrophysical Journal*, 896(1):30, 2020.
- [16] Richard Anantua, Sean Ressler, and Eliot Quataert. On the comparison of AGN with GRMHD simulations: I. Sgr A* . , 493(1):1404–1418, March 2020.
- [17] Richard Anantua, Angelo Ricarte, George Wong, Razieh Emami, Roger Blandford, Lani Oramas, Hayley West, Joaquin Duran, and Brandon Curd. On the Comparison of AGN with GRMHD Simulations - II. M87. , 528(1):735–756, feb 2024.
- [18] Faical Ait Benkhali, Nachiketa Chakraborty, and Frank M Rieger. Complex gamma-ray behavior of the radio galaxy m 87. *Astronomy & Astrophysics*, 623:A2, 2019.
- [19] Roger D Blandford and Roman L Znajek. Electromagnetic extraction of energy from kerr black holes. *Monthly Notices of the Royal Astronomical Society*, 179(3):433–456, 1977.
- [20] Gregory Breit and John A Wheeler. Collision of two light quanta. *Physical Review*, 46(12):1087, 1934.
- [21] Bradley W Carroll and Dale A Ostlie. *An introduction to modern astrophysics*. Cambridge University Press, 2017.
- [22] Benjamin DG Chandran, Francois Foucart, and Alexander Tchekhovskoy. Heating of accretion-disk coronae and jets by general relativistic magnetohydrodynamic turbulence. *Journal of Plasma Physics*, 84(3):905840310, 2018.

- [23] Koushik Chatterjee and Ramesh Narayan. Flux eruption events drive angular momentum transport in magnetically arrested accretion flows. *The Astrophysical Journal*, 941(1):30, 2022.
- [24] E Churazov, M Brüggén, CR Kaiser, H Böhringer, and W Forman. Evolution of buoyant bubbles in m87. *The Astrophysical Journal*, 554(1):261, 2001.
- [25] Jason Dexter. A public code for general relativistic, polarised radiative transfer around spinning black holes. *Monthly Notices of the Royal Astronomical Society*, 462(1):115–136, 2016.
- [26] Joshua C Dolence, Charles F Gammie, Monika Mościbrodzka, and Po Kin Leung. Grmonty: a monte carlo code for relativistic radiative transport. *The Astrophysical Journal Supplement Series*, 184(2):387, 2009.
- [27] EHT MWL Science Working Group, J. C. Algaba, J. Anczarski, K. Asada, M. Baloković, S. Chandra, Y. Z. Cui, A. D. Falcone, M. Giroletti, C. Goddi, K. Hada, D. Haggard, S. Jorstad, A. Kaur, T. Kawashima, G. Keating, J. Y. Kim, M. Kino, S. Komossa, E. V. Kravchenko, T. P. Krichbaum, S. S. Lee, R. S. Lu, M. Lucchini, S. Markoff, J. Neilsen, M. A. Nowak, J. Park, G. Principe, V. Ramakrishnan, M. T. Reynolds, M. Sasada, S. S. Savchenko, K. E. Williamson, Event Horizon Telescope Collaboration, Kazunori Akiyama, Antxon Alberdi, Walter Alef, Richard Anantua, Rebecca Azulay, Anne-Kathrin Baczko, David Ball, John Barrett, Dan Bintley, Bradford A. Benson, Lindy Blackburn, Raymond Blundell, Wilfred Boland, Katherine L. Bouman, Geoffrey C. Bower, Hope Boyce, Michael Bremer, Christiaan D. Brinkerink, Roger Brissenden, Silke Britzen, Avery E. Broderick, Dominique Brogiere, Thomas Bronzwaer, Do-Young Byun, John E. Carlstrom, Andrew Chael, Chi-Kwan Chan, Shami Chatterjee, Koushik Chatterjee, Ming-Tang Chen, Yongjun Chen, Paul M. Chesler, Ilje Cho, Pierre Christian, John E. Conway, James M. Cordes, Thomas M. Crawford, Geoffrey B. Crew, Alejandro Cruz-Orsorio, Jordy Davelaar, Mariafelicia de Laurentis, Roger Deane, Jessica Dempsey, Gregory Desvignes, Jason Dexter, Sheperd S. Doeleman, Ralph P. Eatough, Heino Falcke, Joseph Farah, Vincent L. Fish, Ed Fomalont, H. Alyson Ford, Raquel

Fraga-Encinas, Per Friberg, Christian M. Fromm, Antonio Fuentes, Peter Galison, Charles F. Gammie, Roberto García, Olivier Gentaz, Boris Georgiev, Roman Gold, José L. Gómez, Arturo I. Gómez-Ruiz, Minfeng Gu, Mark Gurwell, Michael H. Hecht, Ronald Hesper, Luis C. Ho, Paul Ho, Mareki Honma, Chih-Wei L. Huang, Lei Huang, David H. Hughes, Shiro Ikeda, Makoto Inoue, Sara Issaoun, David J. James, Buell T. Jannuzi, Michael Janssen, Britton Jeter, Wu Jiang, Alejandra Jiménez-Rosales, Michael D. Johnson, Taehyun Jung, Mansour Karami, Ramesh Karuppusamy, Mark Kettenis, Dong-Jin Kim, Jongsoo Kim, Junhan Kim, Jun Yi Koay, Yutaro Kofuji, Patrick M. Koch, Shoko Koyama, Michael Kramer, Carsten Kramer, Cheng-Yu Kuo, Tod R. Lauer, Aviad Levis, Yan-Rong Li, Zhiyuan Li, Michael Lindqvist, Rocco Lico, Greg Lindahl, Jun Liu, Kuo Liu, Elisabetta Liuzzo, Wen-Ping Lo, Andrei P. Lobanov, Laurent Loinard, Colin Lonsdale, Nicholas R. MacDonald, Jirong Mao, Nicola Marchili, Daniel P. Marrone, Alan P. Marscher, Iván Martí-Vidal, Satoki Matsushita, Lynn D. Matthews, Lia Medeiros, Karl M. Menten, Izumi Mizuno, Yosuke Mizuno, James M. Moran, Kotaro Moriyama, Monika Moscibrodzka, Cornelia Müller, Gibwa Musoke, Alejandro Mus Mejías, Hiroshi Nagai, Neil M. Nagar, Masanori Nakamura, Ramesh Narayan, Gopal Narayanan, Iniyana Natarajan, Antonios Nathanail, Roberto Neri, Chunchong Ni, Aristeidis Noutsos, Hiroki Okino, Héctor Olivares, Gisela N. Ortiz-León, Tomoaki Oyama, Ferayal Özel, Daniel C. M. Palumbo, Nimesh Patel, Ue-Li Pen, Dominic W. Pesce, Vincent Piétu, Richard Plambeck, Aleksandar Popstefanija, Oliver Porth, Felix M. Pötzi, Ben Prather, Jorge A. Preciado-López, Dimitrios Psaltis, Hung-Yi Pu, Ramprasad Rao, Mark G. Rawlings, Alexander W. Raymond, Luciano Rezzolla, Angelo Ricarte, Bart Ripperda, and Freek Roelofs. Broadband Multi-wavelength Properties of M87 during the 2017 Event Horizon Telescope Campaign. , 911(1):L11, April 2021.

[28] Albert Einstein. Die grundlagen der allgemeinen. *Relativitäts- theorie, Annale der Physic*, 49:769, 1916.

[29] Albert Einstein et al. Zur elektrodynamik bewegter körper. *Annalen der physik*, 17(10):891–921, 1905.

- [30] Razieh Emami, Richard Anantua, Andrew A Chael, and Abraham Loeb. Positron effects on polarized images and spectra from jet and accretion flow models of m87* and sgr a. *The Astrophysical Journal*, 923(2):272, 2021.
- [31] Event Horizon Telescope Collaboration, Kazunori Akiyama, Ezequiel Albentosa-Ruíz, Antxon Alberdi, Walter Alef, Juan Carlos Algaba, Richard Anantua, Keiichi Asada, Rebecca Azulay, Uwe Bach, Anne-Kathrin Baczko, David Ball, Mislav Baloković, Bidisha Bandyopadhyay, John Barrett, Michi Bauböck, Bradford A. Benson, Dan Bintley, Lindy Blackburn, Raymond Blundell, Katherine L. Bouman, Geoffrey C. Bower, Michael Bremer, Roger Brissenden, Silke Britzen, Avery E. Broderick, Dominique Broguiere, Thomas Bronzwaer, Sandra Bustamante, John E. Carlstrom, Andrew Chael, Chi-kwan Chan, Dominic O. Chang, Koushik Chatterjee, Shami Chatterjee, Ming-Tang Chen, Yongjun Chen, Xiaopeng Cheng, Ilje Cho, Pierre Christian, Nicholas S. Conroy, John E. Conway, Thomas M. Crawford, Geoffrey B. Crew, Alejandro Cruz-Orsorio, Yuzhu Cui, Brandon Curd, Rohan Dahale, Jordy Davelaar, Mariafelicia De Laurentis, Roger Deane, Jessica Dempsey, Gregory Desvignes, Jason Dexter, Vedant Dhruv, Indu K. Dihingia, Sheperd S. Doeleman, Sergio A. Dzib, Ralph P. Eatough, Razieh Emami, Heino Falcke, Joseph Farah, Vincent L. Fish, Edward Fomalont, H. Alyson Ford, Marianna Foschi, Raquel Fraga-Encinas, William T. Freeman, Per Friberg, Christian M. Fromm, Antonio Fuentes, Peter Galison, Charles F. Gammie, Roberto García, Olivier Gentaz, Boris Georgiev, Ciriaco Goddi, Roman Gold, Arturo I. Gómez-Ruiz, José L. Gómez, Minfeng Gu, Mark Gurwell, Kazuhiro Hada, Daryl Haggard, Ronald Hesper, Dirk Heumann, Luis C. Ho, Paul Ho, Mareki Honma, Chih-Wei L. Huang, Lei Huang, David H. Hughes, Shiro Ikeda, C. M. Violette Impellizzeri, Makoto Inoue, Sara Issaoun, David J. James, Buell T. Jannuzi, Michael Janssen, Britton Jeter, Wu Jiang, Alejandra Jiménez-Rosales, Michael D. Johnson, Svetlana Jorstad, Adam C. Jones, Abhishek V. Joshi, Taehyun Jung, Ramesh Karuppusamy, Tomohisa Kawashima, Garrett K. Keating, Mark Kettinis, Dong-Jin Kim, Jae-Young Kim, Jongsoo Kim, Junhan Kim, Motoki Kino, Jun Yi Koay, Prashant Kocherlakota, Yutaro Kofuji, Patrick M. Koch, Shoko Koyama, Carsten Kramer,

Joana A. Kramer, Michael Kramer, Thomas P. Krichbaum, Cheng-Yu Kuo, Noemi La Bella, Sang-Sung Lee, Aviad Levis, Zhiyuan Li, Rocco Lico, Greg Lindahl, Michael Lindqvist, Mikhail Lisakov, Jun Liu, Kuo Liu, Elisabetta Liuzzo, Wen-Ping Lo, Andrei P. Lobanov, Laurent Loinard, Colin J. Lonsdale, Amy E. Lowitz, Ru-Sen Lu, Nicholas R. MacDonald, Jirong Mao, Nicola Marchili, Sera Markoff, Daniel P. Marrone, Alan P. Marscher, Iván Martí-Vidal, Satoki Matsushita, Lynn D. Matthews, Lia Medeiros, Karl M. Menten, Izumi Mizuno, Yosuke Mizuno, Joshua Montgomery, James M. Moran, Kotaro Moriyama, Monika Moscibrodzka, Wanga Mulaudzi, Cornelia Müller, Hendrik Müller, Alejandro Mus, Gibwa Musoke, Ioannis Myserlis, Hiroshi Nagai, Neil M. Nagar, Dhanya G. Nair, Masanori Nakamura, Gopal Narayanan, Iniyana Natarajan, Antonios Nathanail, Santiago Navarro Fuentes, Joey Neilsen, Chunchong Ni, Michael A. Nowak, Junghwan Oh, Hiroki Okino, Héctor Raúl Olivares Sánchez, Tomoaki Oyama, Feryal Özel, Daniel C. M. Palumbo, Georgios Filippou Paraschos, Jongho Park, Harriet Parsons, Nimesh Patel, Ue-Li Pen, Dominic W. Pesce, Vincent Piétu, Aleksandar PopStefanija, Oliver Porth, Ben Prather, Giacomo Principe, Dimitrios Psaltis, Hung-Yi Pu, Venkatesh Ramakrishnan, Ramprasad Rao, Mark G. Rawlings, and Luciano Rezzolla. The persistent shadow of the supermassive black hole of M87: II. Model comparisons and theoretical interpretations. , 693:A265, January 2025.

[32] Event Horizon Telescope Collaboration, Kazunori Akiyama, Antxon Alberdi, Walter Alef, Keiichi Asada, Rebecca Azulay, Anne-Kathrin Baczko, David Ball, and Mislav et al. Baloković. First M87 Event Horizon Telescope Results. I. The Shadow of the Supermassive Black Hole. , 875(1):L1, April 2019.

[33] Gregory Eyink, Ethan Vishniac, Cristian Lalescu, Hussein Aluie, Kalin Kanov, Kai Bürger, Randal Burns, Charles Meneveau, and Alexander Szalay. Flux-freezing breakdown in high-conductivity magnetohydrodynamic turbulence. *Nature*, 497(7450):466–469, 2013.

[34] José A. Font. Numerical Hydrodynamics in General Relativity. *Living Reviews in Relativity*, 3(1):2, December 2000.

- [35] Valeri P Frolov and Andrei Zelnikov. *Introduction to black hole physics*. OUP Oxford, 2011.
- [36] Charles F Gammie, Jonathan C McKinney, and Gábor Tóth. Harm: a numerical scheme for general relativistic magnetohydrodynamics. *The Astrophysical Journal*, 589(1):444, 2003.
- [37] RG Giovanelli. Magnetic and electric phenomena in the sun's atmosphere associated with sunspots. *Monthly Notices of the Royal Astronomical Society*, 107(4):338–355, 1947.
- [38] Mike Guidry. *Modern general relativity: black holes, gravitational waves, and cosmology*. Cambridge University Press, 2019.
- [39] Kazuhiro Hada, Akihiro Doi, Kiyooki Wajima, Filippo D'Ammando, Monica Orienti, Marcello Giroletti, Gabriele Giovannini, Masanori Nakamura, and Keiichi Asada. Collimation, acceleration, and recollimation shock in the jet of gamma-ray emitting radio-loud narrow-line seyfert 1 galaxy 1h0323+ 342. *The Astrophysical Journal*, 860(2):141, 2018.
- [40] Kazuhiro Hada, Jong Ho Park, Motoki Kino, Kotaro Niinuma, Bong Won Sohn, Hyun Wook Ro, Taehyun Jung, Juan-Carlos Algaba, Guang-Yao Zhao, Sang-Sung Lee, et al. Pilot kava monitoring on the m 87 jet: Confirming the inner jet structure and superluminal motions at sub-pc scales. *Publications of the Astronomical Society of Japan*, 69(4):71, 2017.
- [41] Gregory G Howes. A prescription for the turbulent heating of astrophysical plasmas. *Monthly Notices of the Royal Astronomical Society: Letters*, 409(1):L104–L108, 2010.
- [42] John David Jackson. *Classical electrodynamics*. John Wiley & Sons, 2021.
- [43] Roy P. Kerr. Gravitational Field of a Spinning Mass as an Example of Algebraically Special Metrics. , 11(5):237–238, September 1963.
- [44] J-Y Kim, TP Krichbaum, R-S Lu, E Ros, U Bach, M Bremer, P De Vicente, M Lindqvist, and JA Zensus. The limb-brightened jet of m87 down to the 7 schwarzschild radii scale. *Astronomy & Astrophysics*, 616:A188, 2018.

- [45] Shinji Koide, David L Meier, Kazunari Shibata, and Takahiro Kudoh. General relativistic simulations of early jet formation in a rapidly rotating black hole magnetosphere. *The Astrophysical Journal*, 536(2):668, 2000.
- [46] Malcolm S Longair. *High energy astrophysics*. Cambridge university press, 2011.
- [47] Ru-Sen Lu, Keiichi Asada, Thomas P Krichbaum, Jongho Park, Fumie Tazaki, Hung-Yi Pu, Masanori Nakamura, Andrei Lobanov, Kazuhiro Hada, Kazunori Akiyama, et al. A ring-like accretion structure in m87 connecting its black hole and jet. *Nature*, 616(7958):686–690, 2023.
- [48] Jose Maria Martí and Ewald Müller. Numerical Hydrodynamics in Special Relativity. *Living Reviews in Relativity*, 2(1):3, December 1999.
- [49] Jonathan C McKinney and Roger D Blandford. Stability of relativistic jets from rotating, accreting black holes via fully three-dimensional magnetohydrodynamic simulations. *Monthly Notices of the Royal Astronomical Society: Letters*, 394(1):L126–L130, 2009.
- [50] John Michell. On the Means of Discovering the Distance, Magnitude, &c. of the Fixed Stars, in Consequence of the Diminution of the Velocity of Their Light, in Case Such a Diminution Should be Found to Take Place in any of Them, and Such Other Data Should be Procured from Observations, as Would be Farther Necessary for That Purpose. By the Rev. John Michell, B. D. F. R. S. In a Letter to Henry Cavendish, Esq. F. R. S. and A. S. *Philosophical Transactions of the Royal Society of London Series I*, 74:35–57, January 1784.
- [51] M Mościbrodzka and Charles F Gammie. ipole–semi-analytic scheme for relativistic polarized radiative transport. *Monthly Notices of the Royal Astronomical Society*, 475(1):43–54, 2018.
- [52] Monika Mościbrodzka, Heino Falcke, and Hotaka Shiokawa. General relativistic magnetohydrodynamical simulations of the jet in m 87. *Astronomy & Astrophysics*, 586:A38, 2016.

- [53] Monika Mościbrodzka, Charles F Gammie, Joshua C Dolence, Hotaka Shiokawa, and Po Kin Leung. Radiative models of sgr a* from grmhd simulations. *The Astrophysical Journal*, 706(1):497, 2009.
- [54] Ramesh Narayan, Igor V Igumenshchev, and Marek A Abramowicz. Magnetically arrested disk: an energetically efficient accretion flow. *Publications of the Astronomical Society of Japan*, 55(6):L69–L72, 2003.
- [55] Ramesh Narayan, Aleksander Sądowski, Robert F Penna, and Akshay K Kulkarni. Grmhd simulations of magnetized advection-dominated accretion on a non-spinning black hole: role of outflows. *Monthly Notices of the Royal Astronomical Society*, 426(4):3241–3259, 2012.
- [56] Daniel CM Palumbo, George N Wong, and Ben S Prather. Discriminating accretion states via rotational symmetry in simulated polarimetric images of m87. *The Astrophysical Journal*, 894(2):156, 2020.
- [57] Eric S Perlman, John A Biretta, William B Sparks, F Duccio Macchetto, and J Patrick Leahy. The optical-near-infrared spectrum of the m87 jet from hubble space telescope observations. *The Astrophysical Journal*, 551(1):206, 2001.
- [58] Eric S. Perlman, R. E. Mason, Christopher Packham, N. A. Levenson, Moshe Elitzur, Justin J. Schaefer, Masatoshi Imanishi, William B. Sparks, and James Radomski. The Mid-Infrared Emission of M87. , 663(2):808–815, July 2007.
- [59] MA Prieto, JA Fernández-Ontiveros, S Markoff, D Espada, and O González-Martín. The central parsecs of m87: jet emission and an elusive accretion disc. *Monthly Notices of the Royal Astronomical Society*, 457(4):3801–3816, 2016.
- [60] Eliot Quataert and Andrei Gruzinov. Turbulence and particle heating in advection-dominated accretion flows. *The Astrophysical Journal*, 520(1):248, 1999.
- [61] George B Rybicki and Alan P Lightman. *Radiative Processes in Astrophysics*. John Wiley & Sons, 1979.

- [62] Barbara Ryden and Bradley M Peterson. *Foundations of astrophysics*. Cambridge University Press, 2020.
- [63] Aleksander Sądowski, Ramesh Narayan, Alexander Tchekhovskoy, and Yucong Zhu. Semi-implicit scheme for treating radiation under m1 closure in general relativistic conservative fluid dynamics codes. *Monthly Notices of the Royal Astronomical Society*, 429(4):3533–3550, 2013.
- [64] K. Schwarzschild. On the Gravitational Field of a Mass Point According to Einstein’s Theory. *Abh. Konigl. Preuss. Akad. Wissenschaften Jahre 1906,92, Berlin,1907*, 1916:189–196, January 1916.
- [65] George Gabriel Stokes. On the composition and resolution of streams of polarized light from different sources. *Transactions of the Cambridge Philosophical Society*, 9:399, 1852.
- [66] Maciek Wielgus, Kazunori Akiyama, Lindy Blackburn, Chi-kwan Chan, Jason Dexter, Sheperd S Doleman, Vincent L Fish, Sara Issaoun, Michael D Johnson, Thomas P Krichbaum, et al. Monitoring the morphology of m87* in 2009–2017 with the event horizon telescope. *The Astrophysical Journal*, 901(1):67, 2020.
- [67] AS Wilson and Y Yang. Chandra x-ray imaging and spectroscopy of the m87 jet and nucleus. *The Astrophysical Journal*, 568(1):133, 2002.
- [68] Ricardo Yarza, George N Wong, Benjamin R Ryan, and Charles F Gammie. Bremsstrahlung in grmhd models of accreting black holes. *The Astrophysical Journal*, 898(1):50, 2020.
- [69] Feng Yuan and Ramesh Narayan. Hot accretion flows around black holes. *Annual Review of Astronomy and Astrophysics*, 52(1):529–588, 2014.
- [70] Vladimir Zhdankin, Dmitri A Uzdensky, Gregory R Werner, and Mitchell C Begelman. Electron and ion energization in relativistic plasma turbulence. *Physical review letters*, 122(5):055101, 2019.

VITA

Hayley West grew up in Schererville, Indiana and always had a drive for understanding the universe. She obtained her bachelor's degree from the University of Florida in Gainesville, Florida in 2022 where she began her theoretical astrophysics research in galactic evolution. She went on to complete a year-long internship in Rosman, NC where she worked on radio instrumentation to observe active galactic nuclei. After, she attended the University of Texas - San Antonio to complete a master's degree in Physics studying the mechanics of black holes. Her future ambitions will be to complete a PhD in the field of physics continuing research into the chaotic nature of plasma that surrounds the highest-energy phenomena in the universe.